UNIVERSITAT POLITÈCNICA DE CATALUNYA
BARCELONATECH

Escola Superior d'Enginyeries Industrial, Aeroespacial i Audiovisual de Terrassa

Study of the passive flow control mechanism applied to a generic (DrivAer) car

Author:
Rubén González Viera

Director:
Ivette María Rodríguez Pérez

Co-Director:
Manel Soria Guerrero

Bachelor's Degree Thesis

Bachelor's Degree in Aerospace Vehicle Engineering

Escola Superior d'Enginyeries Industrial, Aeroespacial i Audiovisual de Terrassa
Universitat Politècnica de Catalunya

January 17, 2021

Acknowledgements

Firstly, I would like to thank my parents Josep González and Montse Viera, whose guidance, support and encouragement throughout my life have made this study possible. I also want to thank my brother Marc, as without him, this work could not have been possible either.

Secondly, I would like to appreciate my grandparents, relatives and friends for always being there when needed.

Additionally, I would like to acknowledge Ivette María Rodríguez Pérez for directing me during this project, and all the professors that during my student's life have guided me.

Finally, I would like to thank God for making this study possible, providing me the wisdom, strength and the people already mentioned throughout my life.

Contents

List of Figures

List of Tables

Nomenclature

μ	Dynamic viscosity
ν	Kinematic viscosity
ρ	Density
τ	Shear stress
τ_w	Wall shear stress
C_d	Drag coefficient
C_f	Skin friction coefficient
C_l	Lift coefficient
C_p	Pressure coefficient
CAD	Computer aided design
CFD	Computational fluid dynamics
D	Drag
g	Gravity
L	Lift
LES	Large Eddy Simulation
p	Pressure
$RANS$	Reynolds Averaged Navier-Stokes

Re	Reynolds number
S	Area
U	Speed
u_τ	Friction velocity
VG	Vortex generator

Abstract

From this last ten years on, the last trend of the automotive industry has been to produce daily driver cars as efficient as possible. This decision has permitted aerodynamic performance to be one of the most important aspects in a car's development. From slender designs, through the implementation of splitters or diffusers and right up to deployable spoilers at certain speeds, there are multiple aerodynamic components. However, when this elements are mentioned, nobody thinks of vortex generators, those geometries located on the car's roof, usually with a shark fin design. At first, one could think they only are used as covers, while the reality is far from that.

In this work, a study of these vortex generators will be carried out, from the design of several geometries to its aerodynamic behaviour, to finally understand if their implementation is purely aesthetic or if they indeed improve the vehicle's aerodynamic performance.

Aim

The aim of this project is the aerodynamic study of the DrivAer car, focusing on improving its performance by the addition of passive flow control mechanisms such as vortex generators, widely used nowadays by the automotive sector.

Scope

The project will include the following items:

- Theoretical study of the current car aerodynamics, focusing on its aerodynamic components.
- Overview of the current turbulence models, and the subsequent choice of a RANS method based on the DrivAer configuration.
- CAD design of different vortex generator types.
- Mesh generation for each CAD file by the pre/post-processing software ANSA.
- Aerodynamic study through CFD and the open source software OpenFOAM.
- Results visualization through the post-processing software ParaView and Matlab.
- A data analysis to provide the vortex generator effects.

Requirements

In order to fulfill the project demands, a set of requirements must be satisfied:

- Regarding the car geometry, the Institute of Aerodynamics and Fluid Mechanics at Technische Universität Munchen offers a variety of configurations for the DrivAer car. Among all of them, the setup chosen has to be as close to a real car geometry as possible. However, as this study will focus on the vortex generators, the engine bay flow has been dismissed. Concerning the model dimensions, a scaled 1:2.5 model is used, so no further post-processing is required for a comparison with the experimental data.
- The simulations must be carried out by the following conditions:
  - Incompressible flow.
  - Turbulent flow.
  - Newtonian flow.
  - Static geometry.
  - Heat transfer effects will not be considered.

Background

Aerodynamic performance has been sought during the last decades among the automotive groups for various reasons. Most of them come from the competitive side, while the rest arrive from the ordinary one. All in all, a conclusion can be stated: the more aerodynamic performance, the better. Usually, the competitive sector is always seeking for maximum performance, whereas the ordinary tries to adapt those technological advances to the day-to-day necessities such as fuel consumption, for instance. Among all the aerodynamic advances made in the competitive field, the vortex generators have been capable of surpassing that boundary previously commented, being implemented mainly on the car's roof over the last decade. The need of improving the radio antenna has lead to cover them with a vortex generator geometry, not only gaining in the designing aspect but the aerodynamics.

When a person looks for aerodynamic elements in a regular car, spoilers or diffusers are the ones that come across. However, barely anyone notices the vortex generator located on the roof or even in the mirrors in some car models. For this reason, this study focuses on understanding the aerodynamic effects that those geometries produce in cars, and demonstrating if its implementation is only design-oriented.

In order to obtain legitimate results, the approach followed is to be capable of solving a realistic but generic car geometry by CFD. By comparing the experimental results with the data acquired, a turbulence model can be fitted, capable of calculating legitimate aerodynamic data. Afterwards, a vortex generator is added to the car's geometry and then it is solved. The results obtained, therefore, will be legitimate, explaining the vortex generators effects. However, as in every simulation problem, the computational factor is crucial, both in the quality of the results

and the computational time. With the resources available, a tradeoff is done in order to obtain the most realistic results for a reasonable computational time.

Chapter 1

Introduction to automotive aerodynamics

In this first chapter, an introduction to car aerodynamics, also known as automotive aerodynamics, is performed. First of all, a brief overview of the recent history this sector has had will be explained. Then, some aerodynamic concepts will be detailed, such as lift and drag coefficients. Finally, car components related to aerodynamics will be exposed, being spoilers, diffusers and vortex generators among them.

1.1 Historical overview

It is noticeable that over the 20th century, since the first automobiles were mass-produced and installed definitely in the society, their design has changed drastically. Since its origins, the main challenge was to find a reliable power unit to propel the car [15]. Many forms appeared, from electric to internal combustion engines, being this last the ones that finally prevailed during the 20th century. With a reliable power unit, the seek for better specifications started: automobiles needed to be faster, safer, more agile. All in all, better vehicle performance was pursued.

It wasn't until 1920s that engineers began to consider the shape of the automobiles to improve the car aerodynamics. As it will be explained later on, aerodynamic

drag increases with the squared of velocity, and in that time, engines started reaching considerable speeds, producing awful performances. By the 1950s, with the raise of motorsport championships, engineers were systematically analyzing those aerodynamic properties for high performance vehicles [15].

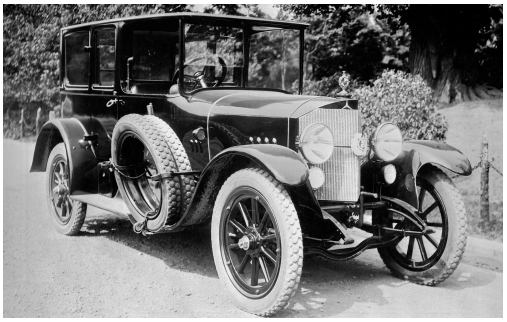

FIGURE 1.1: Mercedes car from 1920 [1]

FIGURE 1.2: Mercedes-Benz 170 S from 1950[1]

For the last decades of the century, the technological advances from the motorsports gradually irrupted in day-to-day automobiles. This meant a subtle change for car manufacturers: efficiency over peak performance, which is directly linked to fuel consumption. Then, automobiles need to perform as good as possible in everyday scenarios, with the corresponding speed spectrum. But, most importantly, they have to excel at fuel consumption, from an economic and environmental point of view. This direction was the one followed a few decades ago and still remains nowadays.

1.2 Aerodynamic forces

The forces originated by the interaction between an airflow and a body are the so-called aerodynamic forces. These are originated by two phenomenons [16]:

- Pressure distribution.
- Shear stress distribution.

where those distributions are located over the surface of a body. This can be mathematically translated as:

$$Force = \int_S (-pn + \tau)\, dS \tag{1.1}$$

The resultant force can be resolved into two components, lift (L) and drag (D).

1.2.1 Lift

Lift is defined perpendicular to the relative velocity between the body and the air, and it is crucial in the aeronautics sector. Mainly, it is the force that compensates weight, making flying possible. Lift is defined as follows:

$$L = \frac{1}{2}\rho v^2 S C_L \tag{1.2}$$

where ρ denotes for density, v denotes for relative air velocity, S denotes for the projected area and C_L denotes for lift coefficient.

In the automobile sector, however, an upwards force is not desirable. Instead, a downwards force or negative lift, also known as downforce, is pursued for a better car stabilization in every situation, that being in corner or high speeds in general.

1.2.2 Drag

Drag is the net force obtained in the air direction. It produces the resistance offered by the airflow against the body movement. It resulting in several losses, being fuel consumption and thus economical losses among them. Drag can be described with the following equation:

$$D = \frac{1}{2}\rho v^2 S C_D \tag{1.3}$$

where the only variable different from the lift's equation 1.2 is the C_D term, denoting the drag coefficient.

It is logic to think that car manufacturers are constantly trying to reduce this force for a better car efficiency, just as mentioned in 1.1.

1.2.3 Moment

From a dynamic point of view, a force being applied from a certain distance generates a moment, and this case is no different. However, this moment is generated due to the location where aerodynamic forces are applied.

It is important to remember that both forces come from pressure distributions. Therefore, they shall be applied in the center of pressure. Even so, lift and drag are applied in the aerodynamic center. Then, this mathematical translation comes with a penalty, a moment has to be added.

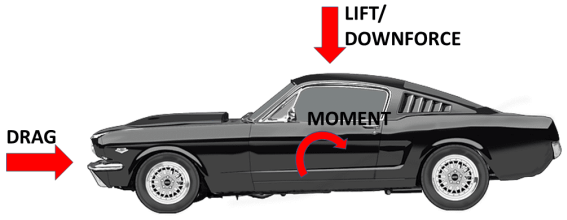

FIGURE 1.3: Lift, drag and moment applied on a car [2]

1.3 Aerodynamic components for cars

Figure 1.3 sums up how aerodynamic forces affect a car. In the previous section, some comments were stated about the necessity of a drag reduction and the generation of downforce for a car's better performance.

In this section, the main car components designed to solve this problem are presented, with a brief description of each ones function. The already mentioned elements are the following:

- Splitters

- Canards
- Side Skirts
- Diffuser
- Spoilers
- Vortex Generators

1.3.1 Splitters

This component is commonly found on the front of the car, and it consists on a flat extension at the very bottom of the front bumper [17]. Splitters are widely used in race cars, although in day-to-day vehicles are not seen at all, being the reason usually each country's regulations. Despite that, motorsports have a justified reason for using splitters: they produce downforce due to a pressure difference between the upper and lower part of the splitter. This downforce is used in several ways. Usually, race cars are rear-wheel drived, then that downforce at the front of the car is used for stabilization.

FIGURE 1.4: Front splitter in Audi S1 [3]

1.3.2 Canards

Also known as dive planes, canards have a geometry similar to spoilers, in the sense that both emulate an aerodynamic profile. Nevertheless, canards are located at

the front bumper, just as the splitters. Both have the same function, producing downforce to the car. In this case though, the purpose of dive planes is fully oriented to shift aerodynamic balance forward or, in other words, stabilization [4].

FIGURE 1.5: Canard on a front bumper [4]

Thanks to their location, there is no need of prominent dive planes producing large forces, because the distance from the center of gravity is the key factor for generating the aerodynamic moment.

1.3.3 Side Skirts

This component is maybe the most versatile one out of all, because depending of its configuration, it has multiple aerodynamic functions. As for the most common configuration is concerned, side skirts are a chassis extension, just as splitters or canards are. The principal difference is their location, being installed on the sides of the car.

FIGURE 1.6: Carbon side skirt [5]

On one hand, the functionality of side skirts is to prevent side air from entering the underbody of tha car. The problem here is that this airflow is slower than the one coming from the front. In addition, it does not follow the same direction. All of it causes energy losses, which results in deceleration [18].

On the other hand, side skirts have also been used in motorsports to improve the ground effect by sealing the underbody of the car. This sealing is achieved by the side skirt's geometry: not only a parallel extension to ground is needed, but the distance from the ground to this extension is also important.

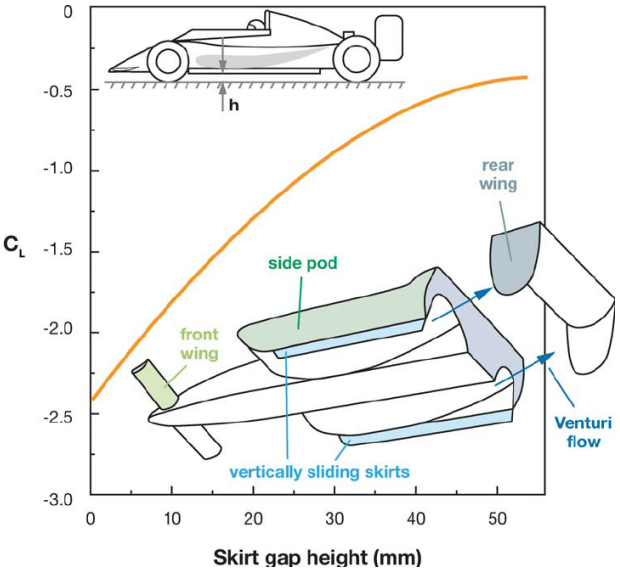

FIGURE 1.7: Side skirts' effect on total downforce [5]

As figure 1.7 shows, in a formula 1 type car (where the ground effect is looked for), the lower the skirt gap's heigth to the ground, the higher the downforce is due to a better underbody sealing.

1.3.4 Diffuser

This element follows the same principle as side skirts or canards, which is creating downforce through accelerating the airflow. In this case, diffusers exploit the flow coming from the underbody of the car.

FIGURE 1.8: Racing car with spoiler and diffuser [6]

As figure 1.8 shows, they are located at the rear bumper of the vehicle, and it is not usual to implement them on everyday cars. As it has been mentioned before, the main purpose is to accelerate the airflow from the underbody of the car, creating a low pressure region compared to the top of the vehicle, creating an aerodynamic grip. Depending on the length of the diffuser walls, as well as the angle they are oriented with, this downforce generated can be controlled, optimizing each car's performance.

1.3.5 Spoilers

Probably the best known aerodynamic component in cars, spoilers are, in essence, an aerodynamic profile upside down. Following the exact same behaviour of the already mentioned elements, the spoiler's bottom part accelerates the airflow coming from the roof's end, generating a pressure difference in the rear of the vehicle and thus, downforce is originated. It is arguably the most effective aerodynamic

component in a car, affecting to a reduction of the aerodynamic lift coefficient up to 32% [19].

As figure 1.8 shows, rear spoilers can have significant sizes, which can lead to an increment of drag. Nevertheless, the stability obtained by the downforce created weights much more in the tradeoff.

1.3.6 Vortex generators

These aerodynamic components were studied initially in aircraft for controlling the boundary layer separation [20]. However, as most of the components mentioned before, it did not take long to implement those advances to the automotive industry (see figure 1.9).

FIGURE 1.9: Vortex generator (Shark fin shape) on top of the BWM 3 series [5]

In order to contextualize the reader for further understanding, a brief summary of the boundary layer separation is described below.

Figure 1.10 describes the velocity profile of a fluid going through a curved surface. In this case, air is the fluid and the surface is a car's roof.

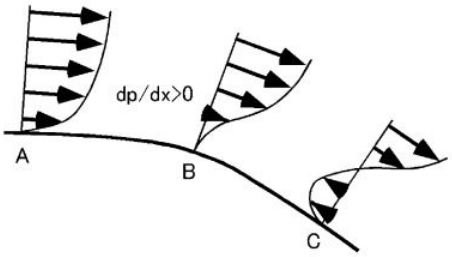

FIGURE 1.10: Air's velocity profile on a curved surface [7]

As the airflow expands towards the end of the surface, the surface sees a reduction in velocity, meaning that the downstream preassure is increasing. Mathematically speaking, an adverse pressure gradient appears, translating into an adverse force emerging from downstream to upstream. Figure 1.10 illustrates perfectly the three stages of this phenomenon: at point A, this adverse pressure gradient is infimum compared to the momentum from the boundary layer, point B (i.e. separation point) is where this adverse pressure gradient is equal to the momentum from the boundary layer, and point C is where the gradient is higher than the momentum.

Returning to the VGs, the purpose of adding them is to supply the momentum from higher regions (where momentum is larger) to lower regions (where momentum is lower). This is achieved by streamwise vortices generated from VGs, located just before the separation point [7]. This effect is represented in figure 1.11.

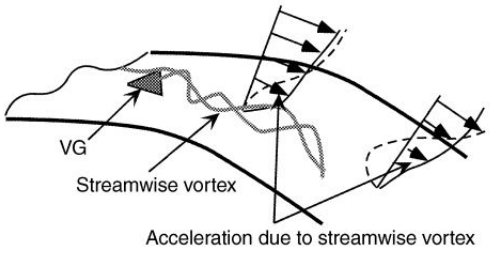

FIGURE 1.11: Vortex generator effect on boundary layer [7]

From figure 1.11 it can also be deduced that the separation point appears further downstream, which is, in the end, the final objective. The air's velocity at this new point will be lower, following its already explained behaviour, and translating

directly into a higher static pressure in this new point compared to the initial one without VGs. As the back pressure increases, the pressure distribution on the totality of the surface is reduced, meaning a reduction in drag. In addition, the separation region is narrowed, which also contributes to a drag decrease.

1.3.6.1 Geometry, number and location

As regards to the geometry, there are different shapes a VG can addapt: delta, shark fin or a bump-shaped type among others. Geometry is crucial because it determines the drag caused by the VG itself.

In addition, the number and location of the VGs also affect on drag reduction (see [7]). It is common to observe racing cars with a stripe with several VGs located on the top end of their roofs, being that the case in figure 1.12

FIGURE 1.12: Strip of VGs on a racing car [8]

FIGURE 1.13: VG located next to the mirror

Besides the roof, there are other locations where this components are positioned, being those next to the mirrors at the vehicle's front, just as in figure 1.13, or at the rear lamps. Both positions have the same purpose explained in the section before. However, the VG located near the mirror has an additional objective, which is to regulate the acoustic levels generated by the airflow. Even though it is an interesting topic, in this work the acoustic aspect of the VGs is not considered.

Chapter 2

Introduction to turbulence models

In this second chapter, an overview of the turbulence models applied in Computational Fluid Dynamics (CFD) is performed. First, a brief description of the Navier-Stokes equations is carried out. Secondly, a brief state of the art regarding the turbulence models is presented, focusing on the RANS models. Finally, the k-ω SST turbulence model, the one used in the simulations for this work, is explained.

2.1 Navier-Stokes equations

This set of partial differential equations describe the motion of viscous fluid substances [21]. In other words, they describe how density, temperature, pressure, viscosity and velocity of a certain fluid interact with each other. The convective form of the Navier-Stokes' momentum equation is shown below:

$$\rho\frac{D\vec{v}}{Dt} = -\nabla p + \rho\vec{g} + \mu\nabla^2\vec{v} + \frac{\mu}{3}(\nabla\cdot\vec{v}) \tag{2.1}$$

Each term in equation 2.1 has a physical meaning [22]:

- $\rho\frac{D\vec{v}}{Dt}$ denotes for convective terms such as acceleration. It represents the inertial forces.

- $-\nabla p$ denotes for pressure forces.
- $\rho\vec{g}$ denotes for massic forces.
- $\mu\nabla^2\vec{v}$ denotes for the viscous friction forces.
- $\frac{\mu}{3}(\nabla\cdot\vec{v})$ denotes for volumetric compression forces.

As far as the fluid is concerned, this equation is valid for compressible newtonian fluids, which manifest a constant viscosity.

Notice how a vectorial notation is used for a compact form. Therefore, a partial differential equation can be obtained for each direction (x, y and z). However, they are too difficult to solved analytically [23]. Nowadays, simulation procedures such as finite volume or finite element methods offer an approximated solution to the problem.

One of the approximations made with the purpose of solving the Navier-Stokes equations are the so called RANS models. Here, the theoretical obtaining of these equations from the originals is shown.

If equation 2.1 is decomposed for one direction results in the following expression:

$$\frac{\partial u_i}{\partial t}+\frac{\partial(u_iu_j)}{\partial x_j}=-\frac{1}{\rho}\frac{\partial p}{\partial x_k}+\nu\frac{\partial^2 u_i}{\partial x_j^2} \tag{2.2}$$

RANS models, whose initials denote for *Reynolds Averaged Navier-Stokes*, part from an assumption that is implicit in its name, which is to decompose the turbulence into a mean and fluctuating component around this mean. Mathematically, this is denoted as follows:

$$u_i=<u_i>+u_i' \tag{2.3}$$

$$<U>\equiv\int_0^\infty u\,dt \tag{2.4}$$

Substituting equations 2.3 and 2.4 into 2.2, the resultant expression is the following:

$$<U_j>\frac{\partial<U_i>}{\partial x_j}=-\frac{1}{\rho}\frac{\partial P}{\partial x_i}+\nu\frac{\partial}{\partial x_j}(\frac{\partial<U_i>}{\partial x_j})+\frac{\partial(-<u_i'u_j'>)}{\partial x_j} \tag{2.5}$$

This new expression results in the obtaining of an additional term named the Reynolds Stress tensor [14], which is defined as:

$$R_{ij} = - < u_i' u_j' > \tag{2.6}$$

For this new term, several hypothesis arise. Among all of them, linear models utilize the Boussinesq assumption. This condition consists of several hypothesis [24]:

- Having a simple relationship between stresses and velocity.
- Gradients through the eddy viscosity.
- Isotropic fluid.

,

This assumption can be expressed mathematically as follows:

$$R_{ij} = - < u_i' u_j' >= 2\nu_t S_{ij} \tag{2.7}$$

where:

$$S_{ij} = \frac{1}{2}(\frac{\partial < U_i >}{\partial x_j} + \frac{\partial < U_j >}{\partial x_i}) \tag{2.8}$$

Finally, adding equations 2.7 and 2.8 to 2.5, the RANS expression is obtained:

$$< U_j > \frac{\partial < U_i >}{\partial x_j} = -\frac{1}{\rho}\frac{\partial P}{\partial x_i} + (\nu + \nu_t)\frac{\partial}{\partial x_j}(\frac{\partial < U_i >}{\partial x_j}) \tag{2.9}$$

2.2 State of the art

Computational fluid dynamics has a major impact in the design of any vehicle in the automotive industry. As it has been already explained in section 1.1, a better performance is requested in today's market, and the improvement in aerodynamics is a feasible solution for overcoming this challenge.

Moving to the technical aspect, the wake of a car is critical in vehicle aerodynamics, mainly due to the recirculation zone created by flow' separation. Therefore, it is mandatory to acknowledge, to comprehend this region in order to design chassis with better aerodynamic performances.

In favor of being aware of this recirculation zone, a CFD simulation is needed to solve the Navier-Stokes equations. For this purpose, several methods are available, but the most widely used in the automotive industry are the following: RANS methods, LES methods and hybrid RANS-LES methods [14]. It is important to remark that a car design, as most of the industrial designs, are submitted to deadlines and economical budgets. Thus, the optimal CFD simulation method is pursued, a method capable of obtaining a reasonable realistic results with the lower computational power needed.

The main advantage of RANS models is the relatively low computational power required. The approach of the model is having an empirical background, even though it is also based on physical phenomenons observed in canonical flows. Therefore, with these two statements in mind, the fidelity of the model is not as high compared to the LES models, for example, but provides a decent approximation for the computational power required [14]. Among all the RANS models, table 2.1 shows some of the most popular in industry.

Concerning the Large Eddy Simulation (LES) models, the idea is filtering fields rather than averaging them. The mesh has to be finer, specially near the walls, because of near-wall effects [25]. The extra refinement causes a notable increment in computational resources, which is its major disadvantage. On the other hand, results are more accurate, particularly in the recirculation region stated before (see [25]).

As RANS models are decent approximations but tend to lack accuracy in the flow separation region, and LES models are precise in this areas but consume too much computational resources, a third model is presented: the Hybrid RANS-LES. The model's concept is to use LES in the separation zone, while RANS is applied elsewhere. Focusing on the boundary layer of the fluid, RANS models do not need a fine mesh in that area, which translates directly to a reduction in the total cell count [14].

To sum up, RANS models use low computational resources and offer a decent precision in certain areas. On the other hand, LES models have a finer mesh, acquiring higher total cell counts and thus a higher computational power is needed. Finally, RANS-LES models use the best of both worlds, optimizing both computational resources and precision in results. Furthermore, table 2.1 presents some of the turbulence models used in the automotive industry, both RANS and RANS-LES hybrid models:

RANS	**Hybrid RANS-LES**
Spalart Allmaras (SA)	SST-DDES
Realisable k - ϵ (RKE)	SST-IDDES
k - ω SST (SST)	SA-DDES
Elliptic Blending k - ϵ $v^2 - f(B - EVM)$	SA-IDDES

TABLE 2.1: Turbulence models used in automotive industry [14]

2.2.1 k - ω SST turbulence model

Once the turbulence models' overview is done, one of them has to be chosen to perform the simulations. In this work, the k - ω SST is the turbulence model selected. First of all, the selection of a RANS model was almost imposed due to the computational resources required by LES or Hybrid models, as well as time deadlines. Then, among all of the remaining models, the k - ω SST is the most suited for the study's purpose, which is the simulation of a car.

The model itself is capable of predicting the separation and reattachment of the fluid with higher fidelity compared to the k-ϵ and the standard k-ω. This improvement comes from how the model works: in far field, the model performs as k-ϵ, while the areas closer to the geometry are solved as a k-ω. Moreover, the model can be applied to those regions where viscosity prevails without further modifications. These regions are too complex for other models such as the Spalart Allmaras [26].

Despite the model's operation, the SST model is probably one of the most widely used to simulate the geometry of this report's case. Therefore, for mesh and model calibrations, it is desirable to already have validated data from other papers.

Finally, the theoretical obtaining of this model is presented, just as with the RANS model. Among all the different SST models, an overview of the standard Menter SST two equation model can be found below.

$$\frac{\partial(\rho k)}{\partial t} + \frac{\partial(\rho u_j k)}{\partial x_j} = P - \beta^* \rho \omega k + \frac{\partial}{\partial x_j}[\,(\mu + \sigma_k \mu_t)\frac{\partial k}{\partial x_j}] \tag{2.10}$$

$$\frac{\partial(\rho\omega)}{\partial t} + \frac{\partial(\rho u_j \omega)}{\partial x_j} = \frac{\gamma}{\nu_t} P - \beta \rho \omega^2 + \frac{\partial}{\partial x_j}[\,(\mu + \sigma_\omega \mu_t)\frac{\partial \omega}{\partial x_j}] + 2(1-F)\frac{\rho \sigma_{\omega 2}}{\omega}\frac{\partial k}{\partial x_j}\frac{\partial \omega}{\partial x_j} \tag{2.11}$$

Equation 2.10 focuses on the k factor, which stands for turbulence kinetic energy. On the other hand, equation 2.11 is based on ω, which denotes for the rate of dissipation of the eddies [27]. For a detailed description of the theoretical part of the k-ω SST model, the author recommends to visit [28], where all the variables and their meaning are posted. There, all the SST models are precisely detailed as well.

Chapter 3

CAD design: DrivAer

In this chapter, the geometry of the generic car used for this study is detailed. The different configurations which the DrivAer offers, the one chosen for the simulations, the scale selected or the final geometry with the addition of the vortex generator are some of the aspects which can be found.

3.1 Drivaer: geometry and configurations

With the upcoming research of car aerodynamics, there was a cohesion problem, since the results were obtained for a different geometry each time. Some of the designs used were even classified by the automotive industries, making knowldegde sharing almost impossible and thus, not advancing in the same direction. Then, the creation of a new realistic generic car model was a must, and that is exactly what the Technische Universität München, in colaboration with the Audi AG and the BMW Group, did. All three came up with the DrivAer, the car geometry that would make car aerodynamics advance.

As a result of this collaboration, the three main car groups in the automotive industry are represented in the 3 configurations the DrivAer has: fastback, notchback and estateback.

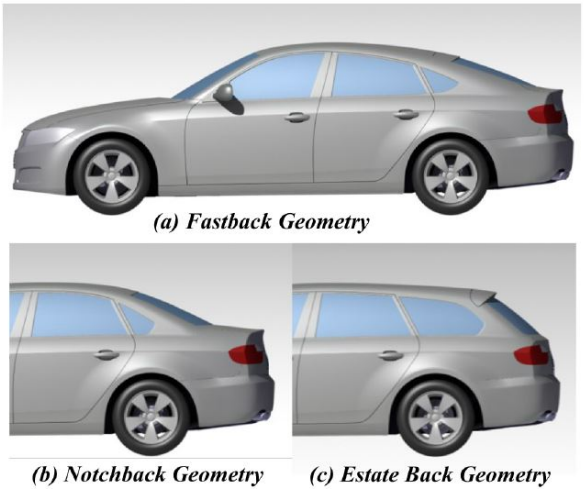

FIGURE 3.1: DrivAer 3 configurations [9]

All three configurations in figure 3.1 can remind you of a mix of two common car designs from the two German brands. It is understandable, because the front part of the DrivAer is based on the Audi-A4, while the rear back is based in the BMW 3 series. It is common sense that both parts take advantage with this usage of their currently car models. On one hand, the Technische Universität München obtains the geometry of a realistic car, and it is capable of sharing the experimental aerodynamic performance of it going through the wind tunnel. On the other hand, the Audi-AG and the BMW Group profit from the possible improvements in aerodynamics from secondary studies being, all in all, a win-win partnership.

Besides the three main configurations, the Technische Universität München also provides subconfigurations in its webpage, in addition to the geometry itself (see reference [29]). This subconfigurations consists of different underbody configurations, the addition of the engine bay flow, the different wheel's type, the exhaust system and, finally, the incorporation of mirrors.

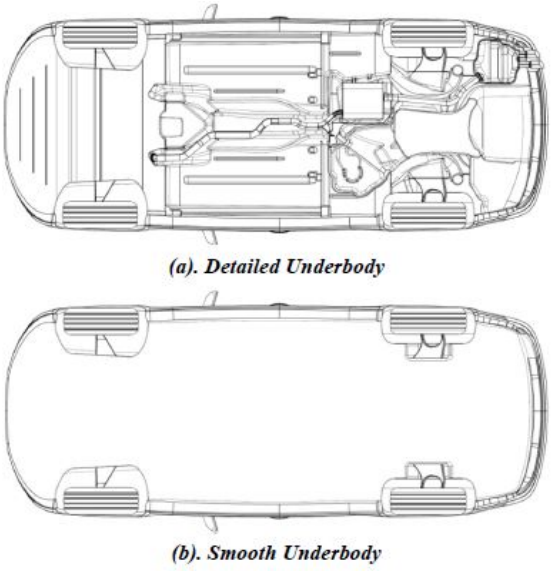

FIGURE 3.2: DrivAer different underbody configurations [9]

As figure 3.2 shows, it is mandatory to define the configuration used for this study, firstly because it delimits the study's work and secondly, and most important, to obtain the corresponding experimental results. Table 3.1 sums up the configuration chosen for this study:

Configuration	**Selection**
Top	Fastback
Body	Standard
Underbody	Smooth
Exhaust system	Standard
Wheels (front & rear)	Smooth
Mirrors	Standard

TABLE 3.1: Selected DrivAer configuration

Notice how the engine bay flow is not added to the geometry. Furthermore, the smoothed configuration has been chosen, prevailing over the detailed one. This statements are due to this study's objectives. The addition of the engine bay has the purpose of carrying out thermal investigations, which is not the goal of this work. Regarding the smoothness, the hole purpose of this investigation is to calibrate a solver with experimental data from the DrivAer, and then to add the vortex generator to see its effects. With the configuration selected, a simplified yet

realistic design is obtained. Moreover, the smoother the disposition is, the more results are found from secondary studies.

Finally, the CAD dimensions from the DrivAer are presented below:

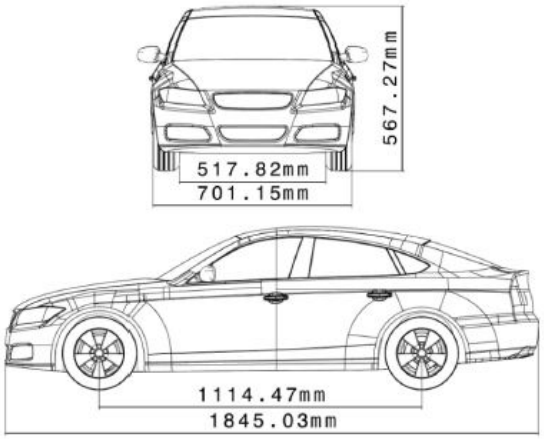

FIGURE 3.3: Main dimensions of the 1:2.5 DrivAer Model [9]

As the DrivAer model was tested in a wind tunnel at Technische Universität München, the researchers opted for a scaled version of 1:2.5, suiting tunnel's capacity. Dimensions like height, depth or wheelbase distance are shown in figure 3.3.

To conclude with the DrivAer CAD design, the actual geometry used in this study is presented below from figures 3.4 to 3.7:

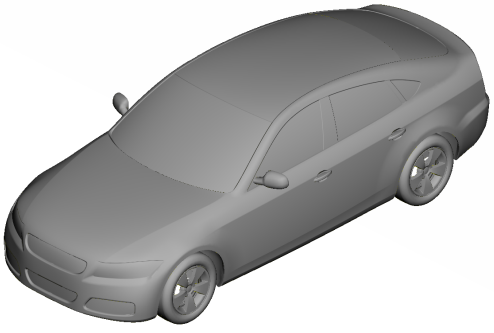

FIGURE 3.4: DrivAer's isometric view

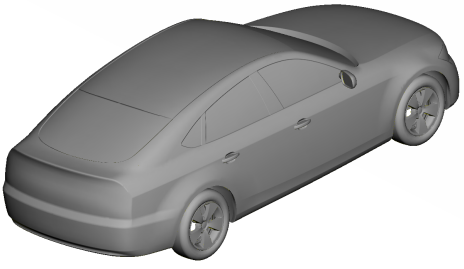

FIGURE 3.5: DrivAer's rear isometric view

FIGURE 3.6: DrivAer's frontal view

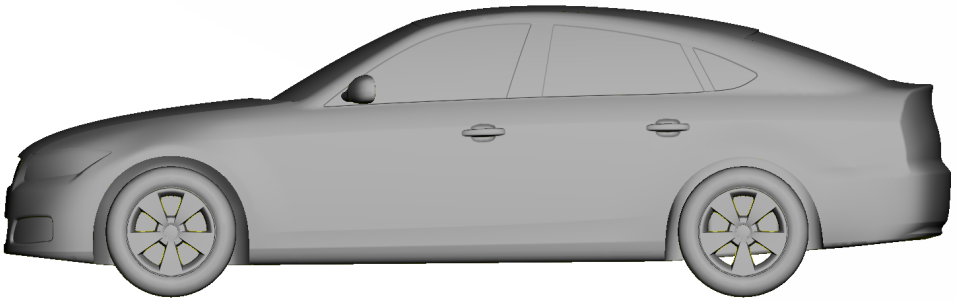

FIGURE 3.7: DrivAer's profile view

3.2 Vortex generator CAD design

As it has been stated in previous sections, the shark fin type is one of the most common vortex generators in the vehicle industry at the moment. Its geometry acts as vortex generator and covers the antenna's electronics both at the same time. In this last topic, it is the solution which provides more space for electronics in its inside.

For this study in particularly, the shark fin's geometry used has been inspired by the *Toyota Corolla 2020*' shape type, shown below:

FIGURE 3.8: Toyota Corolla shark fin profile view

FIGURE 3.9: Toyota Corolla shark fin top view

From figures 3.8 and 3.9 it can be appreciated that the fin, from left to right, increases its section progressively until passed the fin's half. Then, its section starts decreasing until the profiles converge. It can also be noticed how, making a similarity to a wing's geometry, there is an angled surface just at the trailing edge of the fin, which adds space to the electronics and generates a better aerodynamic performance. In order to design the shark fin, certain measurements were carried out, trying to be as precise as possible. All in all, with images 3.8 and 3.9 in mind and fully measured, the CAD design is created:

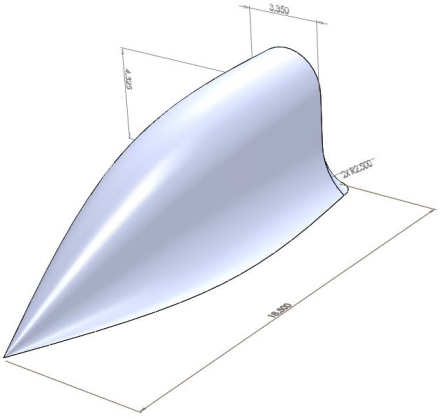

FIGURE 3.10: VG type 1 isometric view

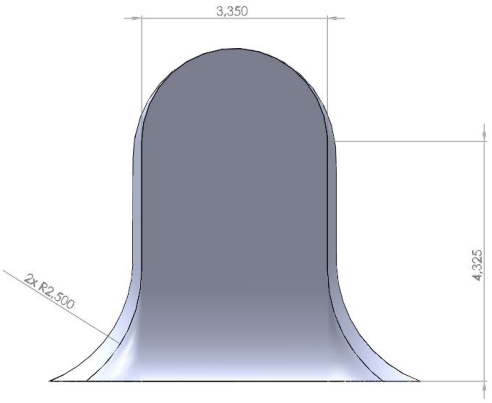

FIGURE 3.11: VG type 1 rear view

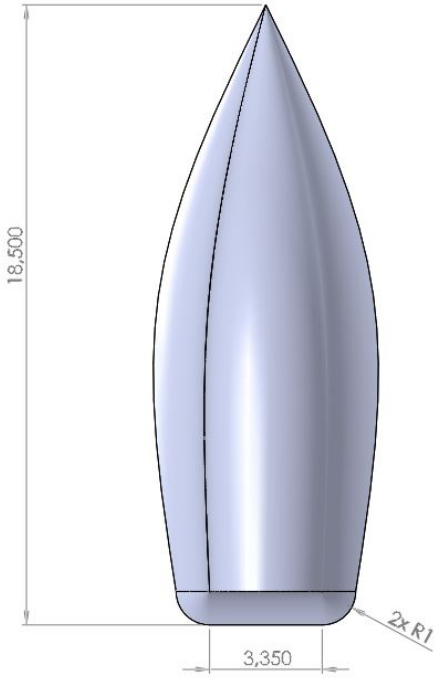

FIGURE 3.12: VG type 1 top view

A small detail can be perceived in figures 3.10, 3.11 and 3.12: all three are designated as type 1. This has a reason being, mentioned in subsection 1.3.6. As the measurments are not perfectly precise, it could happen that the VG' surface is slightly higher than the real surface. Remember that the advantage of adding a VG is to improve the car's aerodynamic performance, i.e. reducing drag and lift. It could occur that the VG' surface is large enough to add more drag than the one reduced by its effect, thus being all this assembly useless.

For that reason, a modification of the original VG is done, modifying the width of the central profile, reducing 1 cm on each side. This zone cannot be reduced as pleasure, electronics have to fit there, as well as a structural problems could appear. Then, more than 1 cm is left for that function. The new VG design, the from now on called VG type 2, is presented below:

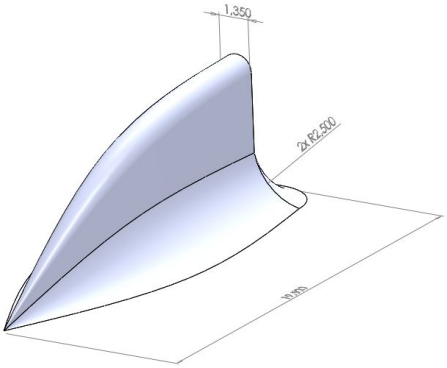

FIGURE 3.13: VG type 2 isometric view

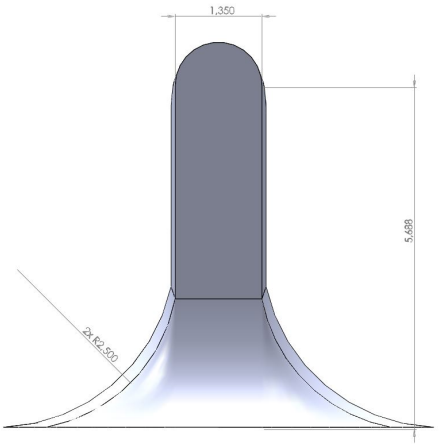

FIGURE 3.14: VG type 2 rear view

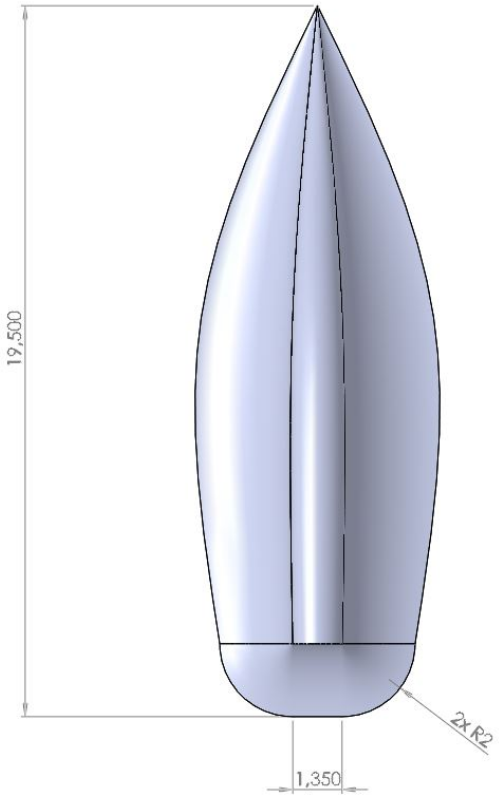

FIGURE 3.15: VG type 2 top view

Finally, the addition of both types of VGs to the DrivAer is performed, and it can be found below the design of the DrivAer with the VG type 2 installed on the roof's end:

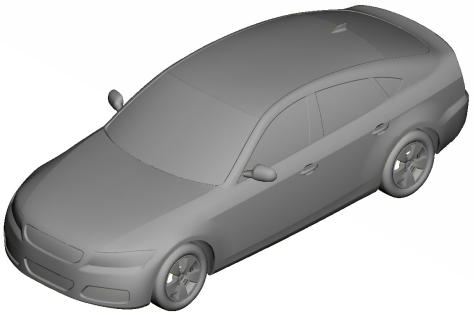

FIGURE 3.16: DrivAer with VG type 2 isometric view

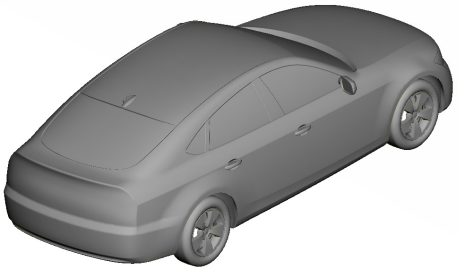

FIGURE 3.17: DrivAer with VG type 2 rear isometric view

FIGURE 3.18: DrivAer with VG type 2 frontal view

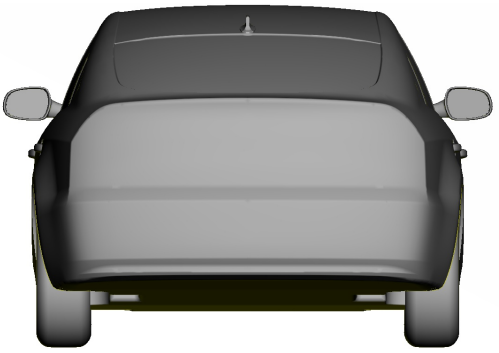

FIGURE 3.19: DrivAer with VG type 2 rear view

FIGURE 3.20: DrivAer with VG type 2 profile view

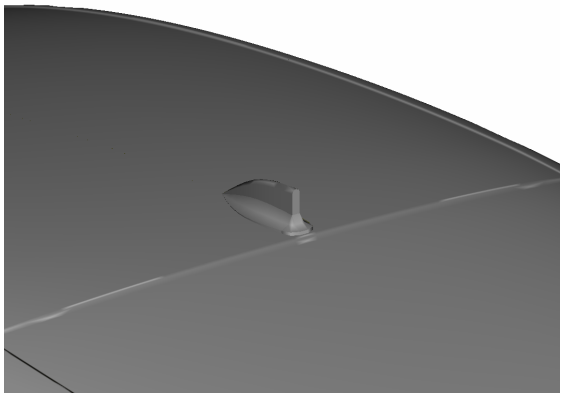

FIGURE 3.21: DrivAer with VG type 2 on the roof zoomed view

To conclude with this third chapter, some comments on the previous images. Firstly, observe how the VG is not visible in figure 3.18. Hence, the frontal area of the car has not changed with the VG's addition. This implies that although the surface of the car has slightly increased by the VG' surface, the area used in the Drag Coefficient (C_d) calculation is the same. This comes from how the C_d is calculated: usually, it is the frontal area the one used in the obtaining of the aerodynamic coefficients in cars [30]. In the end, it results in an advantage based on a mix of the Fastback configuration and the VG's location. However, this configuration will mitigate the VG's effect, but this will be discussed in further chapters.

Finally, the VG is located just at the end of the roof (see figure 3.21), where the surface's curvature is higher, being that the critical spot where the airflow's boundary layer separation is most probably to occur. Therefore, the VG's effect is maximized when located in that zone.

Chapter 4

Preprocess

In this forth chapter, the procedure of preprocessing is explained. In other terms, a description on how the mesh is generated is presented. Firstly, a brief introduction to ANSA, the preprocessing software, is carried out. Secondly, each and every step of the meshing is explained: domain, surface mesh with size boxes, boundary layers with the y+ parameter and volume mesh, ending with a mesh independence commentary for the DrivAer case.

4.1 Mesh generation: ANSA

For this study in particular, the preprocessing software used has been ANSA, from BETA CAE SYSTEMS. ANSA can be described as an advanced multidisciplinary CAE pre-processing tool that provides all the necessary functionality for full-model build up, from CAD data to ready-to-run solver input file, in a single integrated environment [31].

The main advantage over other preprocessing methods is its interface. Its capability to read any kind of CAD format and converting it to ANSA's own language enables geometry optimization for a better simulation. ANSA counts with the TOPO menu, which takes care of the topological aspect. This tool is extremely effective when a geometry clean up is needed. It can smooth corners, fill holes, extrude new geometries, create new surfaces, correct them and a large etc. And,

most importantly, its interface reminds of a conventional CAD program, making it easy to understand and to operate with.

Moreover, it is important to know how ANSA generates a volume mesh. For any volume mesh, the software follows the next steps:

- Domain's creation.
- Vehicle' surface mesh generation.
- Box' surface mesh generation.
- Boundary layers generation.
- Volume mesh generation.

Therefore, the following subsections will follow the same order for a better understanding.

Finally, as the meshing process (in general terms) is exactly the same for both cases (DrivAer with and without VG), the case followed for this step by step explanation is the case without VG. However, images and comments from the VG case will be added when required.

4.1.1 Domain

One important aspect regarding the beginning of any simulation process is to define the domain. In this sense, for this case specifically, mesh dimensions are a mix between [14] and [32].

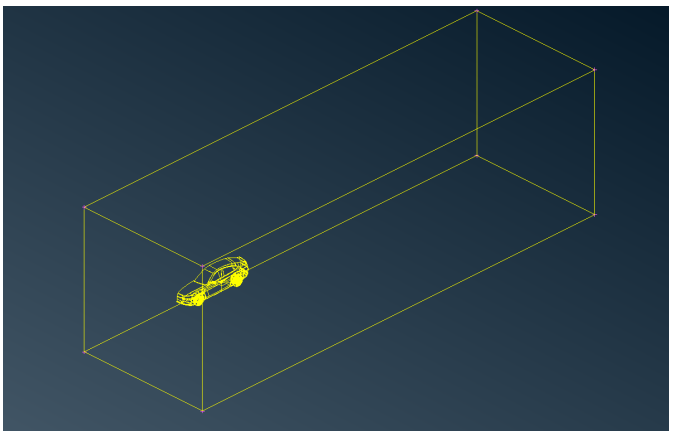

FIGURE 4.1: DrivAer's triangular surface mesh isometric view

Here, the parameter used for most of the domains is the vehicle's height. Concerning this study (see figure 4.1), the front distance, being that the distance between the inlet and the front of the car, is 6H. The rear dimension, which is the distance from the rear bumper to the outlet, is 12H. As for the lateral distance, it is important to mention that the simulation will be performed only with half of the vehicle's geometry, taking advantage of the symmetry existing. Being that said, the lateral dimension, distance from the symmetry plane of the car to the side, is 6H, happening to be the same dimension as the domain's height. All in all, a 1:3 relation has been looked for front and rear dimensions, and a 1:1 relation has been imposed obtaining a squared inlet/outlet. Those assumptions have been completely arbitrary and always between these type of simulations' range.

For this particular case, the 1:2.5 scaled DrivAer model, H equals to 0.567 meters, resulting in the following dimensions (figure 4.1):

Depth (m)	11.317
Width (m)	3.402
Height (m)	3.402

TABLE 4.1: Domain dimensions (m)

4.1.2 Drivaer surface mesh

Once the domain is established, the next step is to mesh the vehicle' surface. For this purpose, ANSA discretizes the model's perimeter, assigning a certain initial element length. Affterwards, it generates a triangular surface mesh with several parameters. The selection of a triangular mesh comes from similarities to other simulations, such as the one seen in [11]. The variables used for this mesh are found in table 4.2:

Parameter	**Value**
Growth rate (1.01 to 2.0)	1.2
Distortion angle	15º
Minimum target length	10 mm
Maximum target length	40 mm
Sharp edges angle limit	20º
Convex sharp edges length	15 mm
Concave sharp edges length	15 mm
Trailing edges angle limit	30º

TABLE 4.2: DrivAer's triangular surface mesh parameters

A clarification about table 4.2: a sharp edge is considered as the perimeter between two macro areas. Therefore, establishing a sharp edge length means that when this macro areas form a certain supplementary angle between them, in this case more than 20º, ANSA assigns to their perimeters a length of 15 mm.

Figures 4.2 and 4.3 illustrate the triangular surface mesh generated with the variables from table 4.2:

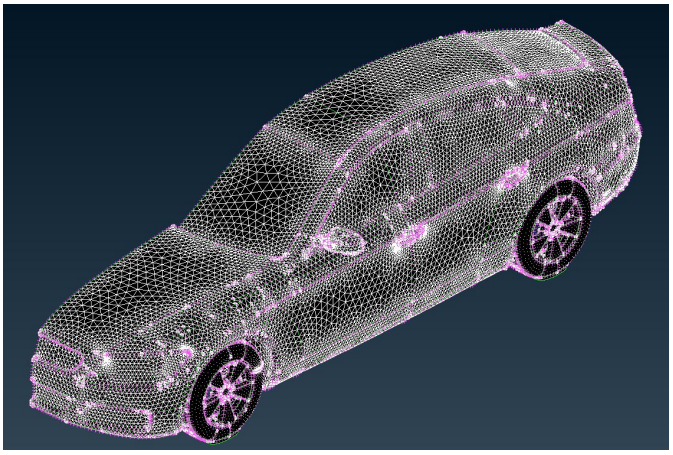

FIGURE 4.2: DrivAer's triangular surface mesh isometric view

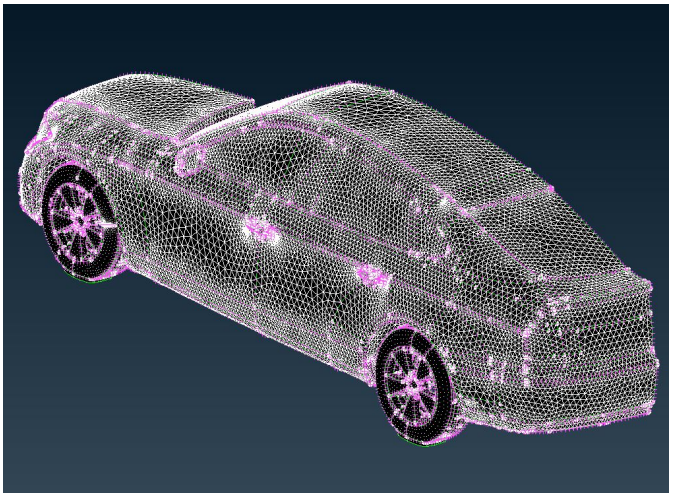

FIGURE 4.3: DrivAer's triangular surface mesh rear isometric view

4.1.3 Box surface mesh

After the vehicle's geometry is meshed, the domain (box) is next. As the triangular mesh type was selected in the previous subsection, it is preferred by the software to use the same mesh type for both the object and the domain surrounding it [11].

Leaving the mesh type apart for a moment, ANSA offers one tool which is extremely helpful for meshing in general, which is the size boxes. This property consists of creating a box with an arbitrary specific size where mesh refinement can be modified independently from the rest. Hence, it allows to create zones with

finer meshes. This is particularly important in this study, because the VG and the vehicle's wake regions need to be finer than the rest of the domain, originating a selective refinement. If this tool was not available, all the domain's mesh would need a higher refinement to perceive the VG's effects, meaning a notable increase in computational resources and time.

Once the utility of the size boxes is explained, the regions where they are located are shown below:

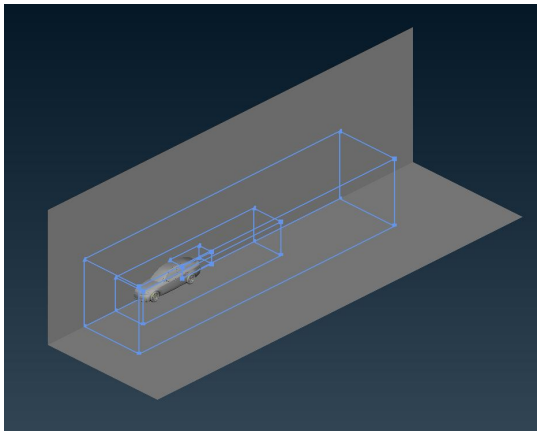

FIGURE 4.4: Size boxes isometric view

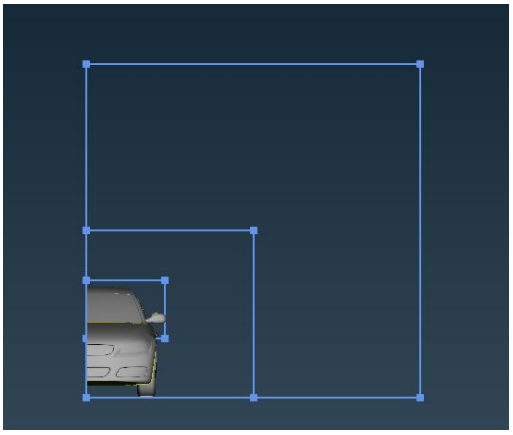

FIGURE 4.5: Size boxes frontal view

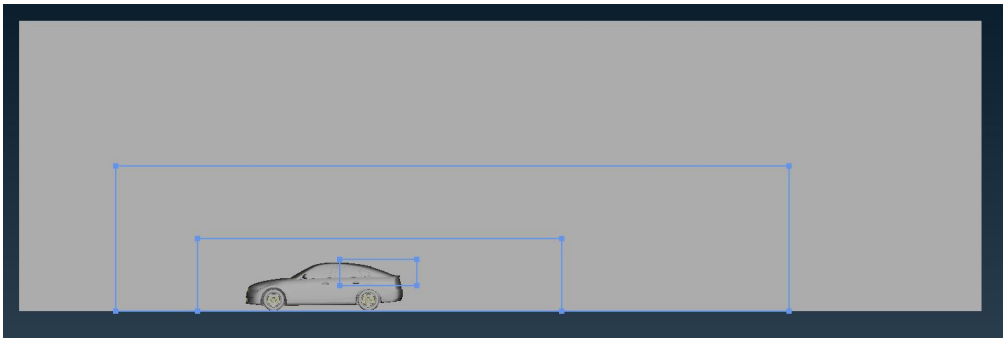

FIGURE 4.6: Size boxes profile view

From figures 4.4, 4.5 and 4.6, several comments can be made. Notice how the first two boxes, ordered from larger to smaller, capture all the vehicle's geometry. The reason behind is that a major refinement is needed where fluid is closer to the car. The second box has as objective to capture the car's wake, while the third one aims for the specific zone where the VG affects the car the most. In addition, the

third box also covers the mirror's wake, a crucial part in car aerodynamics due to the generation of two important vortex on them.

As size is concerned, all the size boxes follow the same criteria as the domain, which is X times H (car's height). For a better understanding, the notation used for the dimension will be the following: XH/XH/YH/ZH/ (distance from frontal bumper, distance from rear bumper, lateral distance from symmetry plane and height distance). Then, all the size boxes' dimensions are detailed below, from larger to smaller:

- Size box 1: 2H/8H/3H/3H.
- Size box 2: H/4H/1.5H/1.5H.
- Size box 3: 2H from frontal bumper to the rear/H (symmetry)/ From H to 2H (height).

As soon as size boxes are defined, the box triangular surface mesh is created. Similar to the procedure followed in 4.1.2, a table is presented below where all the parameters are established for the box mesh.

Parameter	**Value**
Growth rate (1.01 to 2.0)	1.2
Distortion angle	15º
Minimum target length	10 mm
Maximum target length	200 mm
Sharp edges angle limit	30º
Trailing edges angle limit	30º

TABLE 4.3: Box surface mesh parameters

The consequent mesh refinement for the different size boxes is detailed as well in table 4.4:

Name	**Max length surface (mm)**	**Max length volume (mm)**	**Growth rate volume**
Size box 1	60	120	1.2
Size box 2	15	30	1.2
Size box 3	10	15	1.2

TABLE 4.4: Size boxes mesh parameters

It can be observed that in tables 4.3 and 4.4, the size of the elements can change within a designated range: the minimum target length and maximum target length. This condition allows ANSA to adapt the meshing to the problem's necessities. However, if a uniform mesh was desired, i.e. uniform mesh element' size, minimum and maximum target length should be equal.

To conclude, the result of the box meshing can be found below:

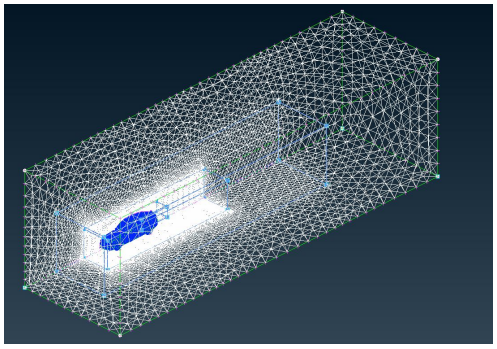

FIGURE 4.7: Box surface mesh isometric view

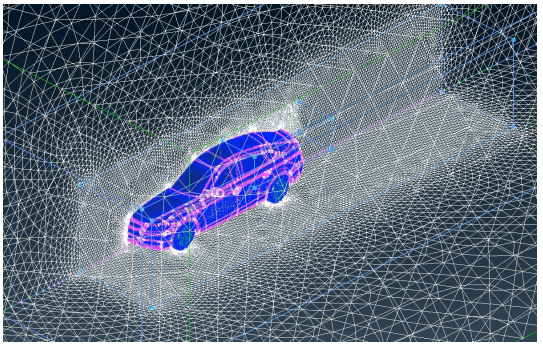

FIGURE 4.8: Box surface mesh isometric view: DrivAer's wake

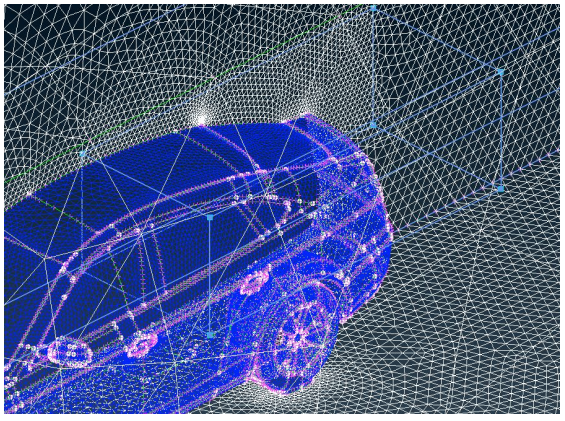

FIGURE 4.9: Box surface mesh isometric view: VG's area (size box 3)

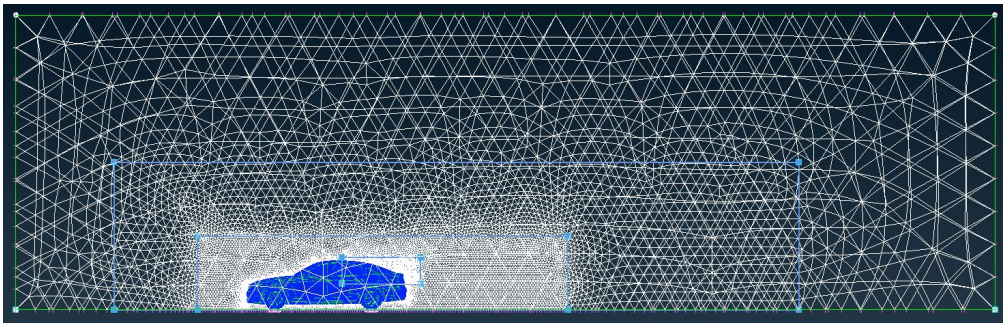

FIGURE 4.10: Box surface mesh profile view

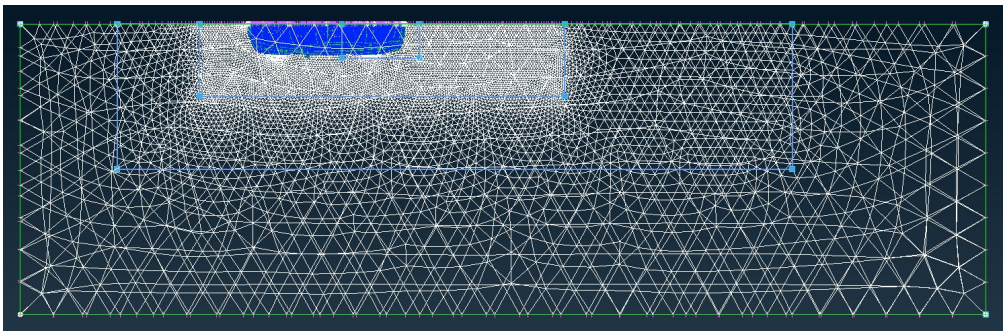

FIGURE 4.11: Box surface mesh top view

It is important to highlight certain aspects from figures 4.7 to 4.11. First of all, the domain is delimited by green lines for a better visualization. Secondly, the DrivAer's triangular surface mesh is also presented in a blue color for the same reason. Moreover, in all the figures can be noticed the size boxes' effect, with a finer mesh in those areas as a result. Finally, the variable element size aspect is mostly observed in figures 4.10 and 4.11.

4.1.4 Y+ parameter

As specified in 4.1, boundary layers should be next. However, it is necessary to understand first the y+ parameter concept first, because they are closely related.

Its importance comes from the near wall areas. As large gradients occur in that region, an accurate representation of the flow in that zone is needed for successful predictions of wall bounded turbulent flows [33], and this is accomplished by using wall functions, and thus the y+ parameter. It is a dimensionless parameter which

allows the calculation of the first cell height (understanding height as the distance from the wall). More precisely, the wall region is meshed using the calculated first cell height value with gradual growth (see figure 4.12). Then, this fact is crucial in how dense/fine a mesh has to be in order to capture the behaviour of the fluid in that zone.

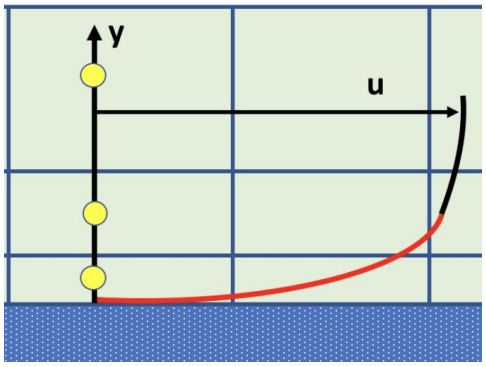

FIGURE 4.12: Logarithmic-based Wall function to resolve boundary layer (in red) [10]

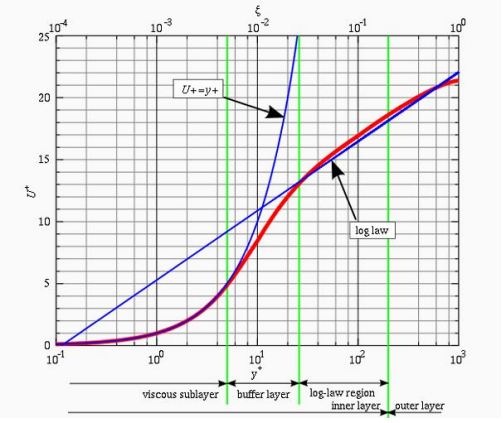

FIGURE 4.13: Law of the wall [10]

But, which number has to equal the y+ parameter in order to do so. The response comes from the wall function (see figure 4.13). The first cell center needs to be placed in the log-law region to ensure the accuracy of the results, which is the range delimited by the two last green vertical lines at the right of figure. This range sets that 30<y+<300 [10]. If the value is below 30, the model cannot be accepted. On the other hand, if it is higher than 300, the solver cannot figure out the outcome of the wall region.

Now that the importance of the y+ parameter has been explained, and a range for its value has been imposed for the simulation's prosperity, an actual calculation of the first cell height is done. For this purpose, the following equations are used:

$$y^+ = \frac{\Delta y \cdot u_\tau}{\nu} \tag{4.1}$$

$$u_\tau = \sqrt{\frac{\tau_w}{\rho}} \tag{4.2}$$

$$\tau_w = \mu \frac{\partial u}{\partial n} \tag{4.3}$$

$$C_f = \frac{\tau_w}{\frac{1}{2}\rho U^2} \tag{4.4}$$

$$u_\tau = U\sqrt{\frac{C_f}{2}} \tag{4.5}$$

$$\frac{C_f}{2} = 0.0359 Re^{-0.2} \tag{4.6}$$

For this study, all variables are imposed by the experimental results except Δy, which denotes for the first cell height. Notice how equation 4.5 is obtained by combining equations 4.2, 4.3 and 4.4. Moreover, expression 4.6 is a C_f commonly used approximation for turbulent flows [34]. Introducing equations 4.6 and 4.5 in equation 4.1 and adding all the variables known, Δy is obtained. Table 4.5 shows all the initial conditions, as well as the results from the previous equations:

Velocity (m/s)	ν **(kg/m-s)**	**Re**	**Cf/2**	u_τ **(m/s)**	**y+**	Δy **(mm)**
40	1.470E-5	4.87E+6	1.65E-3	1.625	30	0.271

TABLE 4.5: Initial conditions and data obtained from the first cell height calculations

Velocity, kinematic viscosity and the Reynolds number are some of the initial conditions extracted from the Technische Universität München wind tunnel's data. All these conditions, in addition to others remaining from the experimental results, will be explained in chapter 5.

In favor of assuring a proper simulation, the *yPlus OpenFOAM function* has been used. Its utility is to represent the y+ parameter all over the vehicle' surface. Hence, regions where the parameter is not valid or not precise enough can be spotted.

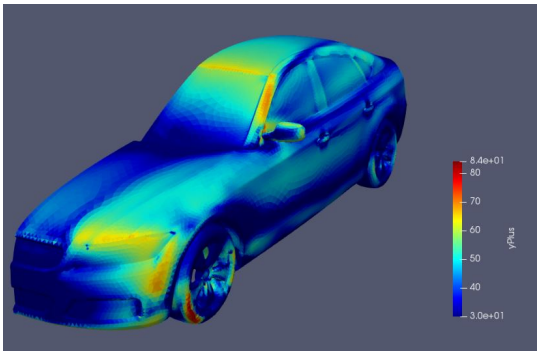

FIGURE 4.14: y+ parameter over the DrivAer's geometry: isometric view.

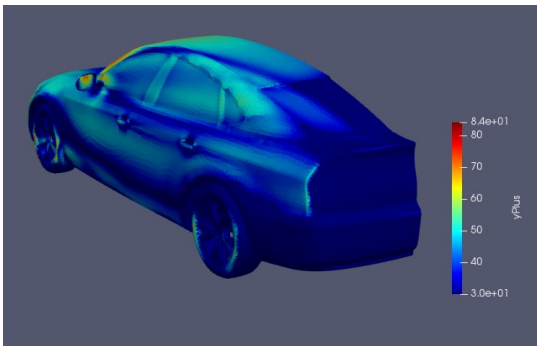

FIGURE 4.15: y+ parameter over the DrivAer's geometry: isometric rear view.

Notice how in figures 4.14 and 4.15 the y+ range is between 30 and 84. Moreover, in figure 4.14 appears the most critical part, the bottom-left of the front tyre, with a maximum value of 84. Other areas such as the head lamp or the A pillar (located next to the driver's position) have also a slightly higher value compared to 30. Finally, some areas are covered in a lighter blue, indicating a y+ from 40 to 50. However, most of the car' surface is covered in dark blue, indicating a predominance of a y+ value of 30. Even though the ideal case would be a surface all covered in dark blue, most of the surface is. As mentioned just before in this section, the acceptance range for an accurate simulation is 30<y+<300. In this case, the range covered for the most part, excluding that tyre area (which is in that acceptance range, and it is even lower than its half), is 30<y+<50, giving validation as regards to the y+ parameter and thus, proper accuracy in the results obtained can be expected.

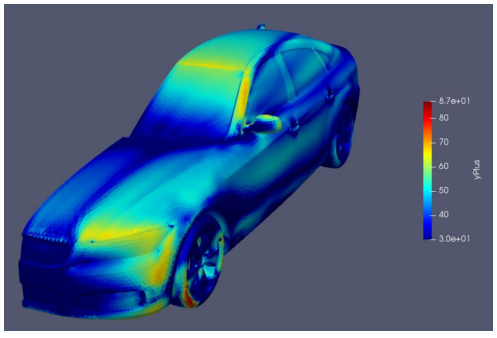

FIGURE 4.16: y+ parameter over the DrivAer's VG geometry: isometric view.

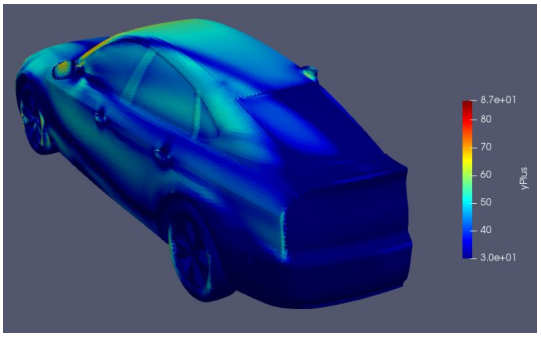

FIGURE 4.17: y+ parameter over the DrivAer's VG geometry: isometric rear view.

As mentioned earlier, the hole meshing process is based on the DrivAer's configuration without the VG. However, when changes appear, even when they are subtle, those modifications are detailed. It is the VG's case, as it is appreciated in figures 4.16 and 4.17, where the maximum y+ value reaches 87, 3 units more than the configuration without VG. Nevertheless, this maximum does not appear in the VG' surface or near by, meaning that this increase is due to a fluctuation of the *yPlus* function, because the DrivAer's original geometry has not been modified.

4.1.5 Boundary layers generation

Probably one of the most useful tools ANSA disposes. It consists of a volume mesh generation with the optimal geometry to catch all the effects from the near wall region. It follows the geometry seen in figure 4.12, and it can be configured independently from the other meshes.

Parameter	**Value**
First height (mm)	0.3
Growth factor	1.2
Number of layers	4
Additional outer layers	3
Last aspect	0.4
Proximity check factor	0.4
Minimum layer aspect	0.1
Maximum layer aspect	1.5

TABLE 4.6: Boundary layers' parameters

In table 4.6 are detailed all the different variables needed for the software to generate those layers. It is important to mention that the first height is slightly higher than the one calculated in table 4.5. The reason is that ANSA has a first height calculator, and introducing the parameters required, the value recommended was 0.3 mm. Moreover, ANSA offers the "additional outer layers" option (see figure 4.18), which is highly recommended. It adds "Y" more layers to the "X" number of layers in absolute mode, so that the last aspect ratio is around 0.4 in this case. This way of layers' generation leads to a very small volume change between the last layer and the first element in the posterior volume meshing [11].

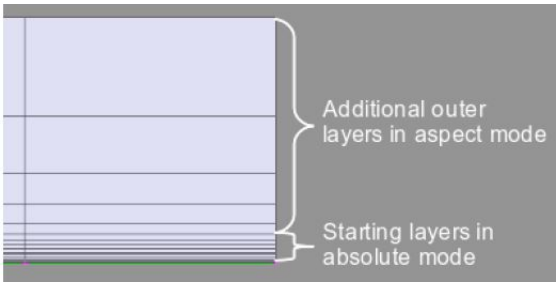

FIGURE 4.18: Additional outer layers' concept [11]

In addition, when the software detects a problematic area for this layers to be created, it automatically regulates the layers' height by the *Squeeze* function. In this way, the volume elements that will be grown later can fit that region [11]. Finally, other parameters such as number of layers or the growth factor have been chosen by similar ANSA simulations such as in [11].

Once the boundary layer parameters and its operation have been detailed, the results on the DrivAer car are presented below in figures 4.19 and 4.20:

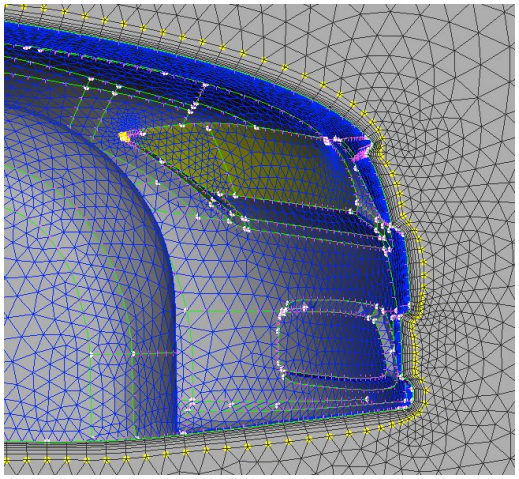

FIGURE 4.19: Boundary layers on DrivAer's geometry: head lamp profile's view

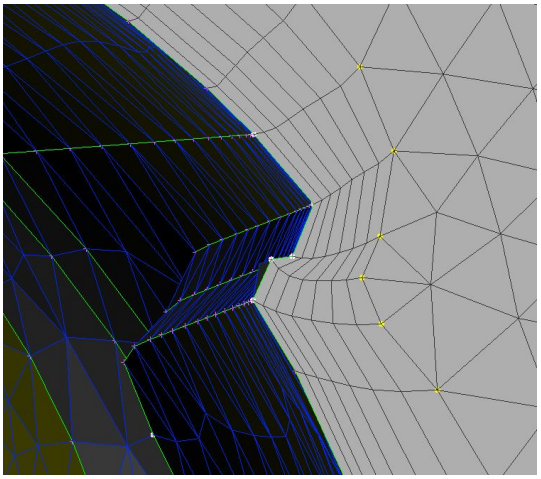

FIGURE 4.20: Boundary layers on DrivAer's geometry: head lamp profile's zoomed view

Although this figures only show one part of the car, the boundary layers surround all the vehicle' surface, as expected. A representative view was looked for due to layers small dimension compared to the model itself.

4.1.6 Volume mesh

The only remaining step for a complete mesh generation in ANSA is the volume mesh. Here, a brief discussion of the meshing algorithms is done, clarifying which is the best model for this study.

First of all, figure 4.21 shows the different algorithms that ANSA disposes for volume meshing:

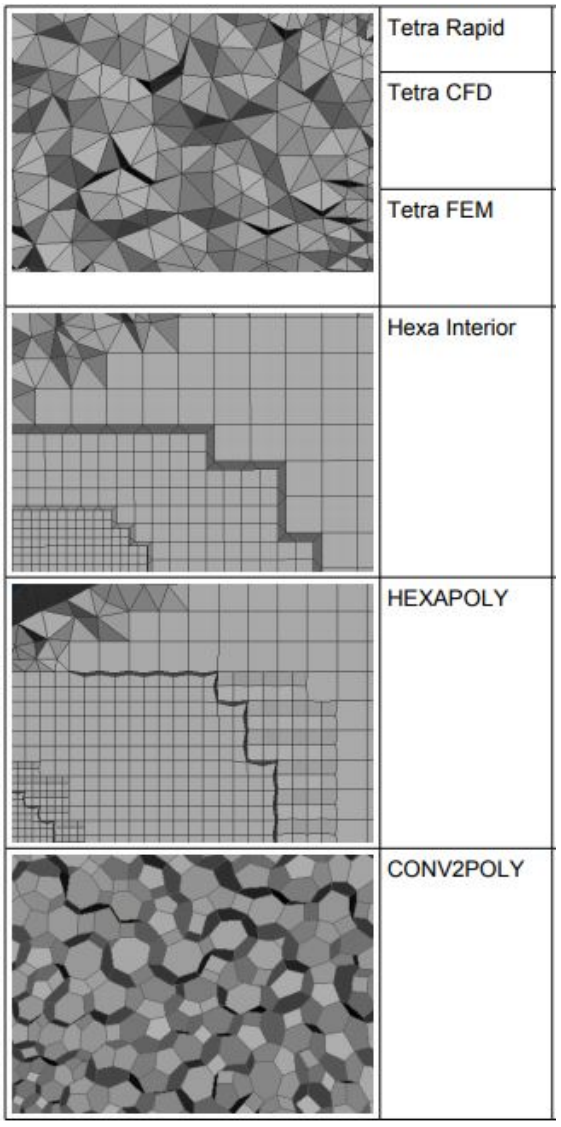

FIGURE 4.21: ANSA's volume meshing algorithms [12]

Now, the following question is which one to pick. As the ANSA CFD guide presents (see [12]), all methods involving tetra elements result in a robust mesh generation. The Tetra Rapid algorithm is recommended for all cases, while the Tetra CFD is suggested with models where large variation in element length is found. Regarding the Tetra FEM, it should be implemented with smaller cases with thin volumes. However, both Tetra CFD and Tetra FEM should only be used if the Tetra Rapid algorithm fails meshing the geometry [12].

Moving to the other three methods, they add a more complex meshing geometry. The Hexa Interior's mesh is conformed by variable hexa elements, with prism and pyramid elements as a transition between those hexa. For the HEXAPOLY, hexa an polyhedral elements vary in size, and the transition elements are polyhedrals and tetras. Finally, the CONV2POLY is a pure polyhedral mesh that can be obtained from any tetra or hybrid mesh [12].

Therefore, with all this information present, the chosen meshing algorithm has to be Tetra. The reason behind is the computational resources. As it will be explained in the mesh independence section, the computational power in this study is limited, and several simulations needed to be done, not only for calibrating the solver, but to simulate the different configurations with the two VGs presented in 3.2. Then, the rest of the methods are discarded, and the three Tetra algorithms remain. Among those three, the Tetra-Rapid is the one selected due to it is faster than the other two. As said earlier, the usage of the other two methods would be necessary if the Tetra-Rapid was not capable of meshing the DrivAer's geometry, which fortunately has not been the case.

Once the volume meshing method is clear, the results are presented below:

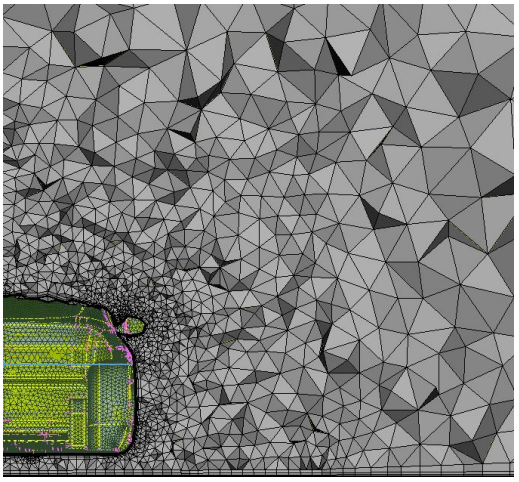

FIGURE 4.22: DrivAer's Tetra-Rapid mesh: sliced view

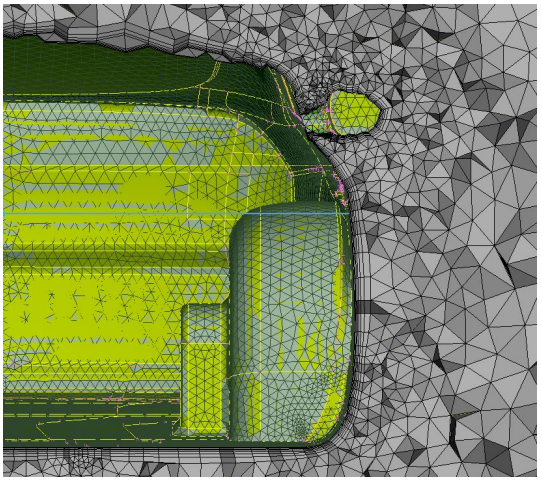

FIGURE 4.23: DrivAer's Tetra-Rapid mesh: sliced view zoomed

Notice how in figure 4.22, the tetra' size variation is notable, meaning that the size boxes (already explained) are doing their job correctly. In addition, the boundary layers generated for the road are observed, as well as the layers created on the vehicle' surface in figure 4.23.

To conclude with the mesh generation section, table 4.7 summarizes the total elements used in all stages (surface, box, boundary layer and volume meshes), together with each element's type:

Shell		**Volume**	
Quads	4466	**Tetras**	840932
Trias	147862	**Pentas**	457982
Total	152328	**Total**	1298914
Mesh total elements: 1451242 ≈ 1.45 million			

TABLE 4.7: DrivAer's total mesh elements without VG

4.1.7 Mesh independence

One aspect that is common in every single simulation study is the mesh independence theme. Accuracy in results is obtained, mainly, by the grade of refinement the mesh has. However, as the discretization of the mesh increases, the computational resources and time needed rise as well. Then, a tradeoff is done in order

to acquire the precision required. The procedure consists of setting an acceptance value. A grand part of the simulations performed in studies do converge, meaning that tend to the theoretical number. Therefore, there would be a point where the improvement of the numerical solution is not worth the extra refinement and thus, the extra computational resources and time needed. In fact, this sweet spot is always looked for in industrial developments, due to its savings in time and resources.

For this work specifically, three meshes were created. All of them had the same properties, only their refinement has been modified. As the DrivAer model disposes of experimental data, the resultant value is known, and can be compared to the numerical results obtained.

Mesh configuration	Shell elements	Volume elements	Total elements	Cd	Error (%)
Type 1	152328	1298914	1451242	0.2740	7.874
Type 2	280384	2975045	3255429	0.2606	2.598
Type 3	301270	3564516	3865786	0.2593	2.087

TABLE 4.8: Data obtained from 3 different mesh configurations

The results obtained in table 4.8 confirm that the finer the mesh, the closer to the real solution the simulation is. This fact can also be seen in figure 4.24, where more refined meshes tend to the experimental value. As concerns to the number of elements, from type 1 configuration to type 2, the refinement has been doubled, and from type 2 to type 3, there has been an increase of almost half a million elements.

As the computational resources are limited, time has been the factor that has changed drastically. For instance, comparing the first two types, simulations have gone from around 2 hours and 30 minutes to 5 hours at least. It is understandable, doubled the elements, doubled the time required. As concerns to type 3 mesh configuration, the final time locates at 6 hours.

Finally, the decisive parameter that has decided the type's election, the error percentage. It was imposed that an error higher than a 5% could not be accepted, as a calibrated model is needed. Then, option 1 is discarded by default. Among the other two options remaining, the already explained tradeoff was applied. Although the last option was more accurate (-0.5% error), it was needed between 45 minutes and 1 hour of extra time for the solver.

Hence, being both valid options regarding the 5% error requirement, and only being a slight improvement of 0.5% in the experimental result, option 2 is the mesh configuration chosen, with 3.2 million elements and a computational time of 5 hours for each simulation.

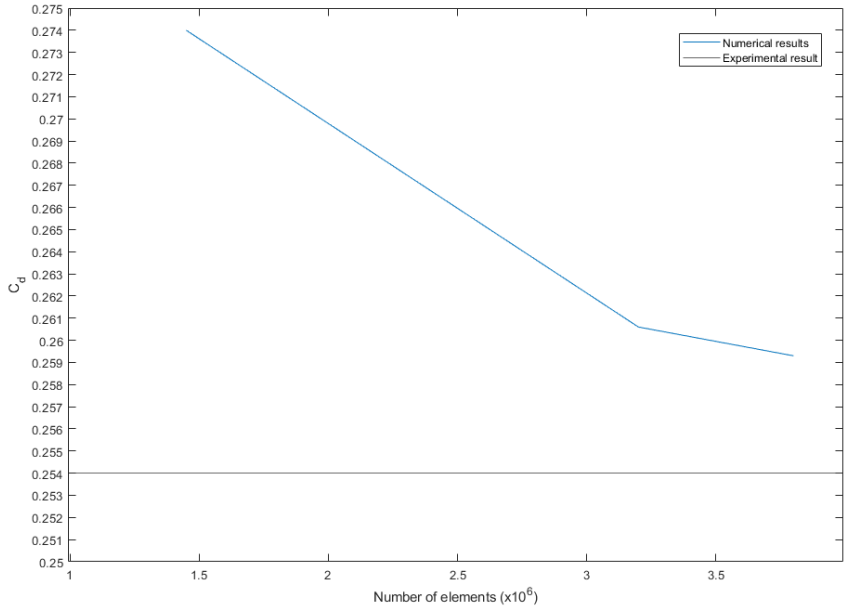

FIGURE 4.24: Mesh Independence graph: refinement / C_d

Chapter 5

Simulation

In this chapter is detailed how the simulation is performed. First, an introduction to OpenFOAM and simpleFOAM is presented. Secondly, a summary of the parameters explained in other chapters, needed for the simulation itself, is found. Finally, the initial conditions for the solver are established.

5.1 OpenFOAM and simpleFoam

Developed primarly by OpenCFD Ltd since early 2000's, OpenFOAM is a free open source CFD software. It is widely common and used in areas like engineering and science. In more detail, OpenFOAM is a C++ toolbox for the development of customized numerical solvers for the solution of continuum mechanics problems [35]. Thus, it has an extensive range of features to solve anything from complex fluid flows involving chemical reactions, turbulence and heat transfer, to acoustics, solid mechanics and electromagnetics [36]. Due to its widely usage, the software is periodically updated to compete against its pay software competitors (Ansys, Nastran, etc.). For this reason, code evaluation, verification and validation is accomplished by a large testing process, assuring the quality OpenFOAM is known for.

Among all the solvers available in OpenFOAM, simpleFoam has been the one chosen. This solver, as its name suggests (Semi-Implicit Method for Pressure Linked Equations), is an algorithm used for solving steady-state incompressible,

turbulent flows. It matches perfectly with the conditions presented in this study, as the case presented meets all these properties. Figure 5.1 shows the algorithm' scheme, where the different steps performed are observed:

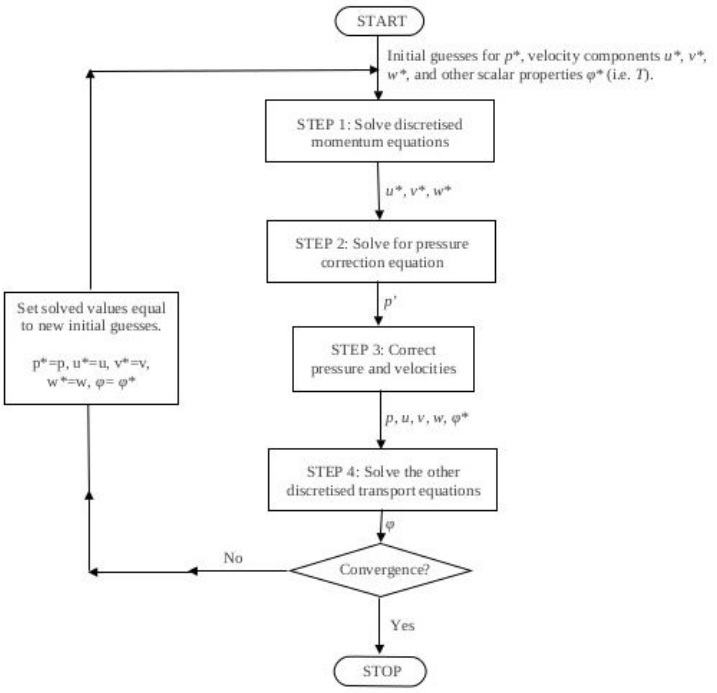

FIGURE 5.1: SIMPLE algorithm' scheme [13]

5.2 Simulation conditions and initial parameters

As it could be deduced, in every simulation study there is a set of conditions and initial parameters that reign the simulation. They are extremely important for a better understanding of the simulation's outcome. For that reason, this section is all about having located all these parameters and conditions.

Starting with the conditions, they are all listed below:

- *Incompressible flow.* Everyday car' speeds are low enough for the flow, in this case air, to be considered as non compressible.
- *Turbulent flow.* The DrivAer's geometry by itself, and all the vehicles' geometry in general, produce turbulent flows.

- *Newtonian flow.* It might be an obvious condition, but without it, all the equations explained regarding fluid mechanics are not valid.

- *Static geometry.* This affects the tyres and wheels of the car. Not having a dynamic mesh saves computational resources, as well as not having a transient problem which complicates the solving. This condition decreases the realistic part of the simulation as regards to the car itself. However, as the purpose is to study the VG's behaviour, the effects of static tyres/wheels are negligible.

- *Heat transfer effects will not be considered.* Similar to the imcompressible's justification, as the airflow is not compressible, heat effects are not relevant for this study. However, if the DrivAer's engine bay configuration was chosen, the exhaust flow could affect the vehicle's wake and thus, heat effects would have to be taken into account.

Following up with the initial parameters, they are all located in table 5.1. All these values have been extracted from papers [14], [9] and [32].

Fluid	**Velocity (m/s)**	**Temperature (°C)**	**Kinematic viscosity** (m^2/s)	**Density** (kg/m^3)	**Reynolds**
Air	40	15	1.47E-5	1.225	4.87E+6

TABLE 5.1: Summary of initial parameters from experimental studies

Finally, some comments on the domain parts are presented. Each face is configured differently depending on its type.

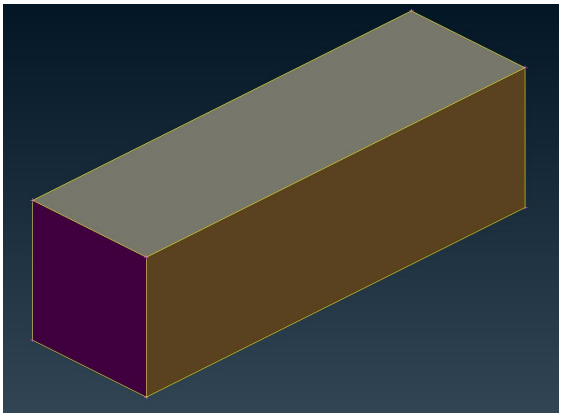

FIGURE 5.2: Domain isometric view

For a better understanding, figure 5.2 shows a domain's isometric view. The different types for each surface are presented below:

- *Inlet/outlet: patch.* Represented in violet color both inlet and outlet.
- *Top, side and symmetry: symmetry.* Top and side are represented in a grey and brownish color respectively. Symmetry is parallel to the side face.
- *Road: wall.* Not visible in 5.2, but it is parallel to the grey face.

5.3 Turbulence parameters

As mentioned in section 2.2.1, the turbulence model used is the k-ω SST. For its usage, and as its name suggests, two parameters are needed for its utilization: k and ω.

However, before its calculation, three more parameters are needed:

- Fluid's velocity (U): 40 m/s.
- Turbulence intensity (I): 1%
- Turbulence length scale (L).

From those 3, only the turbulence length scale needs to be obtained. Both the fluid's velocity and the turbulence intensity are detailed in [14]. Now, turbulence length scale is calculated following the next expression [37]:

$$L = 0.07 \cdot d \tag{5.1}$$

where d denotes for the inlet's diameter or, in this study, the width or height dimension as it is a squared inlet. In section 4.1.1, this value can be found, which is 3.4 meters.

Once this last parameter is calculated, k and ω follow next. In order to do so, the next equations are presented:

$$k = 1.5(U \cdot I)^2 \tag{5.2}$$

$$\omega = \frac{C_{\mu}^{-0.25} k^{0.5}}{L} \tag{5.3}$$

The only unknown variable is C_{μ}, located in equation 5.3. It denotes for a turbulence model constant, and usually has a value of 0.09 [38].

To conclude with this section and thus with this chapter, all the parameters are calculated and can be observed in table 5.2:

d (m)	**L (m)**	**U (m/s)**	**I (%)**	**k** (m^2/s^2)	C_{μ}	ω (s^{-1})
3.4	0.238	40	1	0.240	0.09	3.758

TABLE 5.2: Turbulence parameters

Chapter 6

Results

In this chapter the results from the three different simulations are detailed: the DrivAer standard configuration and the DrivAer with VG's configuration, for both type 1 and 2, seen in 3.2. Moreover, these results will be analyzed in order to observe the effects of the VGs.

6.1 DrivAer standard configuration

In this first section, the calibration of the solver is pursued by simulating the vehicle's normal setup. Then, these values will be compared to the experimental results from the wind tunnel at Technische Universität München. This calibration is usefull not only to add reliability to the solver, but to appreciate the improvement of the aerodynamic performance of the car when VGs are installed.

6.1.1 Mesh convergence

For starters, for the sake of visualizing if the simulation has performed correctly, a checking of its residuals is mandatory. Residuals are used in CFD to see if the solution converges or not. Therefore, its behaviour is critical for a mesh validation.

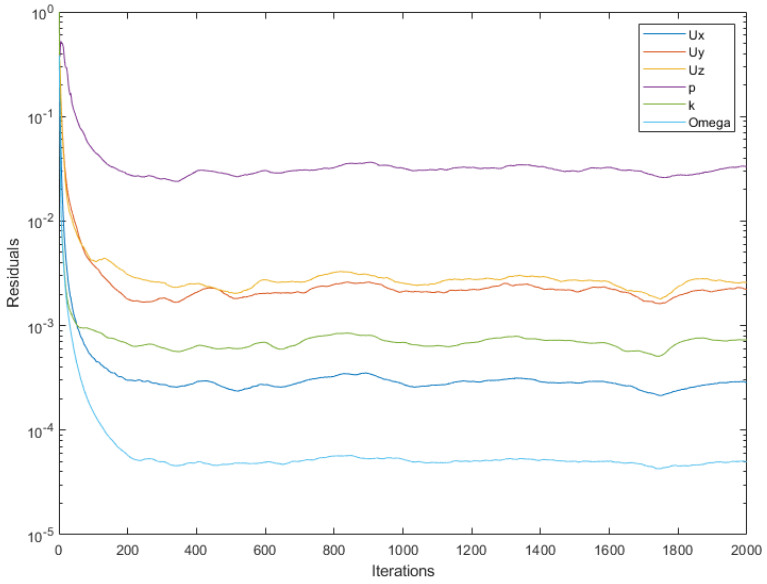

FIGURE 6.1: Residuals from DrivAer standard configuration

For a total of 2000 iterations, the residuals from the velocity (3 components), the pressure (p) and the k and ω parameters are shown in figure 6.1. There, it is observed that the pressure is the only variable which is not under 0.5%, being under 4%. Other variables such as k, Ux or ω are under 0.1 %, meaning that a good convergence is achieved. All in all, the behaviour of the residuals is as expected, obtaining reasonable values for this configuration. Therefore, it can be affirmed that in the simulation, a valid convergence is accomplished.

6.1.2 Aerodynamic performance: C_p, C_l and C_d

Once that the simulation's convergence has been checked, the aerodynamic coefficients are presented below:

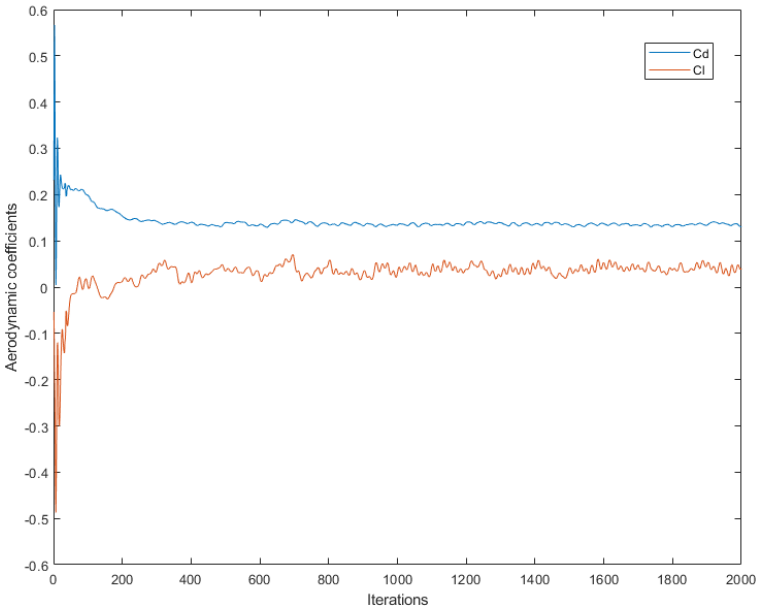

FIGURE 6.2: Aerodynamic coefficients from DrivAer standard configuration

Several aspects need to be mentioned from figure 6.2. First of all, notice how the solver, after a few iterations, tend to converge in the case of the C_d. For the lift coefficient though, it needs more iterations for its convergence, which finally seems to reach.

Aerodynamic coefficients	**Simulation**	**Experimental**	**Error (%)**
C_d	0.2606	0.254	2.598
C_l	0.0788	0.079	0.253

TABLE 6.1: Aerodynamic coefficients data from DrivAer standard configuration

From figure 6.2, the value for each aerodynamic coefficient is obtained, and they can be observed in table 6.1. As mentioned in section 4.1.7, an error under 5% would be a valid number for this study. In this case, both values meet this requirement. Moreover, it is remarkable the accuracy obtained in the lift coefficient, being under 0.5 %.

Despite the value itself, it is important to know the behaviour of the this coefficients over the vehicle's body, so specific areas can be studied. As mentioned in 1.3, not only the value of downforce generated is important, its positioning is crucial too.

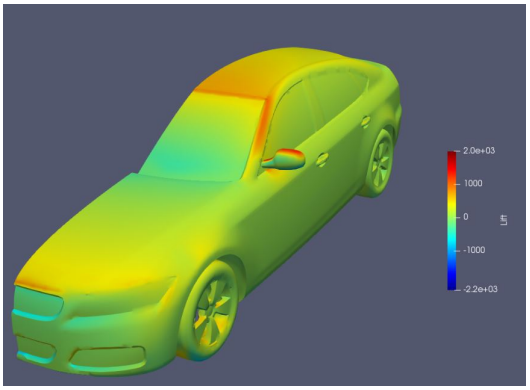

FIGURE 6.3: Lift generated over the DrivAer standard configuration surface, isometric view

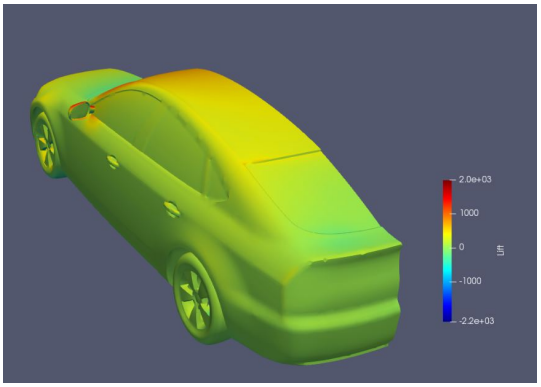

FIGURE 6.4: Lift generated over the DrivAer standard configuration surface, isometric rear view

Notice how figure 6.3 shows that downforce (i.e. negative lift, blueish color) is generated at the front bumper (stagnation point) and over the junction between the bonnet and the windshield, including a significant part of this last one. For front-wheel-drive vehicles, a force pushing to the ground in that location can be beneficial for their stabilization, as their power is transmitted from the engine to the front wheels. In figure 6.4, some downforce is also created over the rear' surface of the car. For racing vehicles, which mostly are rear-wheel-drive, that is the optimal spot for the aerodynamic force to be generated. Exactly as before, rear downforce offers stabilization against the power generated by the rear wheels. All in all, any downforce generated over a car is welcomed, and even better if it is located near the drive-wheels, which is exactly the case.

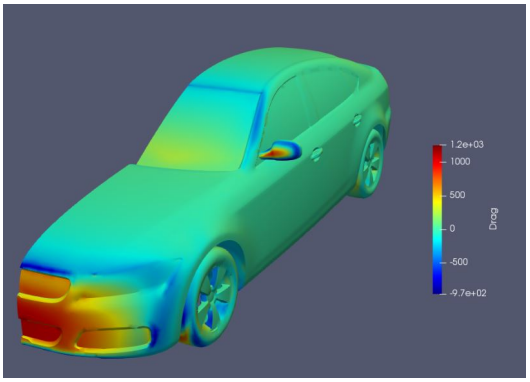

FIGURE 6.5: Drag generated over the DrivAer standard configuration surface, isometric view

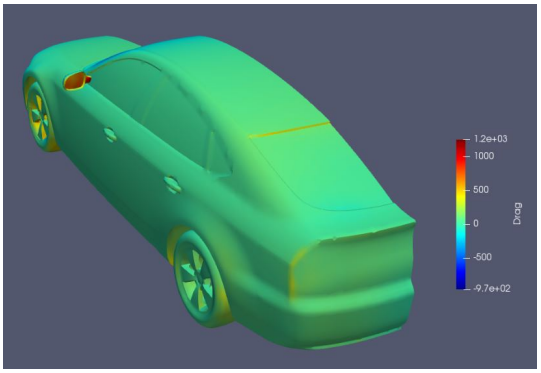

FIGURE 6.6: Drag generated over the DrivAer standard configuration surface, isometric rear view

As drag is concerned, the frontal part of the vehicle is the first one to be in touch with the airflow. Then, it could be expected that the front bumper and the front part of the tyres are the areas where most of the drag is generated (see figure 6.5). It is important to highlight the mirror area, where its behaviour is identical as these front parts due to its position, as it receives an undisturbed airflow. For the rest of the car, figure 6.6 shows that the drag force generated over its surface is uniform, having a relatively low value compared to the parts mentioned earlier.

For a detailed understanding of the conduct of both aerodynamic forces, the pressure coefficient distribution, from which both coefficients (lift and drag) are obtained, has been plotted as function of the car's length. As many cuts can be made to the vehicle's geometry, the symmetry plane has been the one selected to observe this pressure distribution:

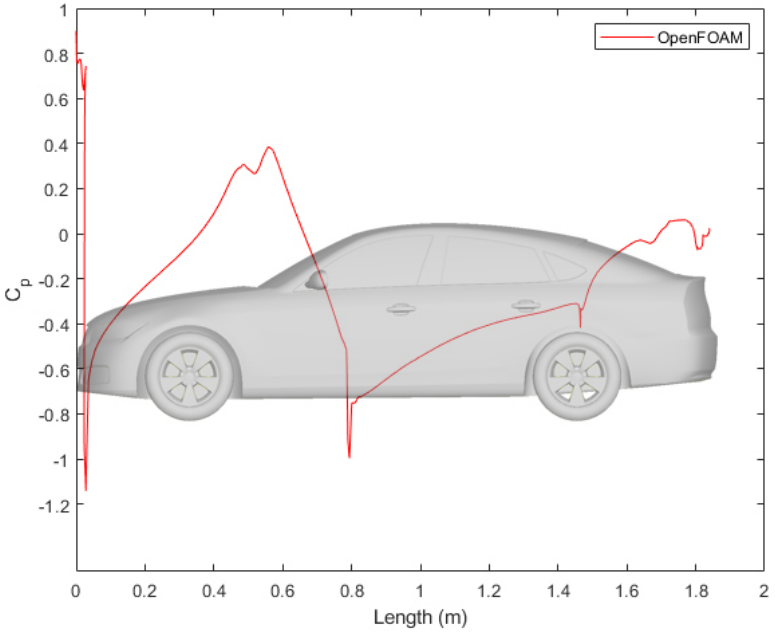

FIGURE 6.7: Pressure coefficient distribution over DrivAer standard configuration symmetry plane

Most of the aerodynamic performance is explained by figure 6.7: C_p starts at 1 just when the airflow reaches the stagnation point, where the velocity is 0. Then a pressure drop occurs at the radiator part of the car due to the air's acceleration, which is observed by the first minimum of the graph. Afterwards, pressure starts

regaining through the car's bonnet until the windshield area, where a maximum is achieved. Notice how there is another peak before this maximum. That top appears thanks to the junction between the bonnet and the windshield. Next, the flow starts accelerating again, losing pressure until the windshield's end, reaching a minimum at 0.8 meters. Then, pressure starts recovering again over the car's roof. Once the step between the roof and the rear part is achieved (length=1.4m approximately), the flow detaches at the end, obtaining a pressure increase. This growth lasts until the furthest trunk area is encountered, where the geometry changes from concave to convex. This explains the last pressure drop at 1.8 meters. Finally, the DrivAer standard configuration almost reaches the ambient pressure, where C_p equals to 0.

However, this behaviour corresponds to the simulated DrivAer standard configuration. Therefore, it is interesting to compare figure 6.7 to the experimental data from [9] and [32]:

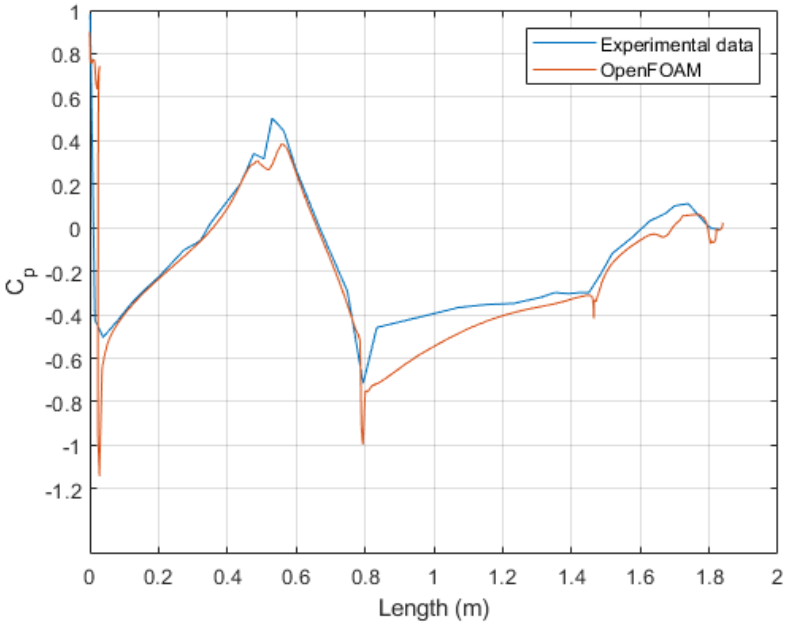

FIGURE 6.8: Pressure coefficient distribution comparison: experimental vs simulated data

As figure 6.8 shows, the model simulated under-predicts the real behaviour of the car. More precisely, there is a notable gap appearing at 0.8 meters (where the windshield finishes) and it starts decreasing until 1.4 meters, where the simulation

performs with its normal deviation. This phenomena occurs due to the wind tunnel configuration [14]. There, a strut-based system is used to hold the DrivAer's body: four of them are found in each wheel, and the final one is located exactly where the windshield ends and the roof starts (see experimental setup in [9]). In the simulation here presented, the wind tunnel's geometry has not been taken into account (besides not being available). Therefore, that gap is caused by the strut's effect on the airflow. Hence, this gap at 0.8 meters is understandable and verifiable, as it appears in other studies (see [14] and [32]), and does not interfere in the validation of the simulation results.

Despite that gap, there is still a difference that can be appreciated, and that is the suction peaks found at the stagnation point and at the windshield's end. Even though [14] explains that the k-ω SST model predicts too strong suction, the deviation is higher than the one supposed by the model usage. As the car's geometry is common, and it is simulated under the same conditions, the only explanation possible is the mesh refinement. Although both volume and surface mesh can be refined, the author believes that a finer surface mesh would be the solution. The reason behind that assumption is the refinement's proportion: in this case, volume mesh is much more refined compared to the surface mesh.

6.2 DrivAer VG configuration: type 1 and type 2

Once the results from the standard setup have been presented, now it is time to install the VG. As mentioned in section 3.2, the VG has a shark fin type geometry. There, two types or configurations are presented: type 1 and 2. This distinction comes from the VG's thickness. In subsection 1.3.6, it is explained that a VG, by its own geometry, can generate the same or more drag than the one reduced by its effect, making the installation useless. Then, the frontal surface of the VG is a crucial factor, translating instantly to the shark fin's thickness. Thus, type 2 has the same VG's geometry but a reduction of the central fin's thickness has been performed (see section 3.2).

For this subsection, only the process of obtaining results for the DrivAer type 2 configuration will be shown to avoid repetitiveness. However, a final section comparing both types is found further on. In addition, the same structure as

for the standard configuration will be followed, starting with the residuals (mesh convergence) and then the aerodynamic performance. Finally, the results of the type 2 configuration will be compared to the ones for the standard configuration, as the idea is to observe any changes in the car's aerodynamic performance.

6.2.1 Mesh convergence

In order to obtain valid results from this new simulation, a study of the mesh convergence is presented by figure 6.9, where the residuals can be observed. It is remarkable the similarity between these two simulations. Only some differences can be spotted, such as the oscillation behaviour, if a finer review is done. Despite that, the residuals are almost identical, having approximately the same values as in figure 6.1. As a reminder, all variables are under 0.5% except the pressure, being around a 4%. With that in mind, it can be affirmed that a valid convergence is achieved.

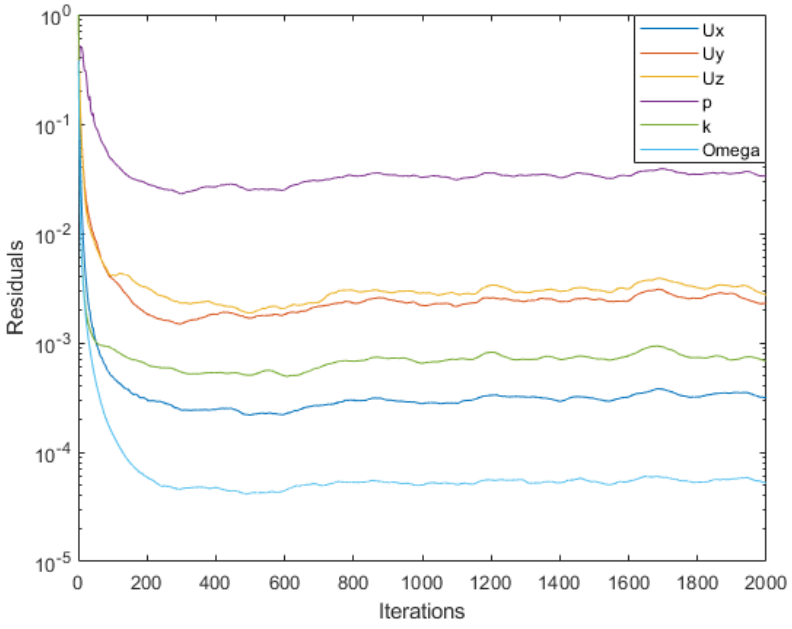

FIGURE 6.9: Residuals from DrivAer VG type 2 configuration

6.2.2 Aerodynamic performance: C_p, C_l and C_d

Making sure that convergence results are viable, the aerodynamic coefficients are presented

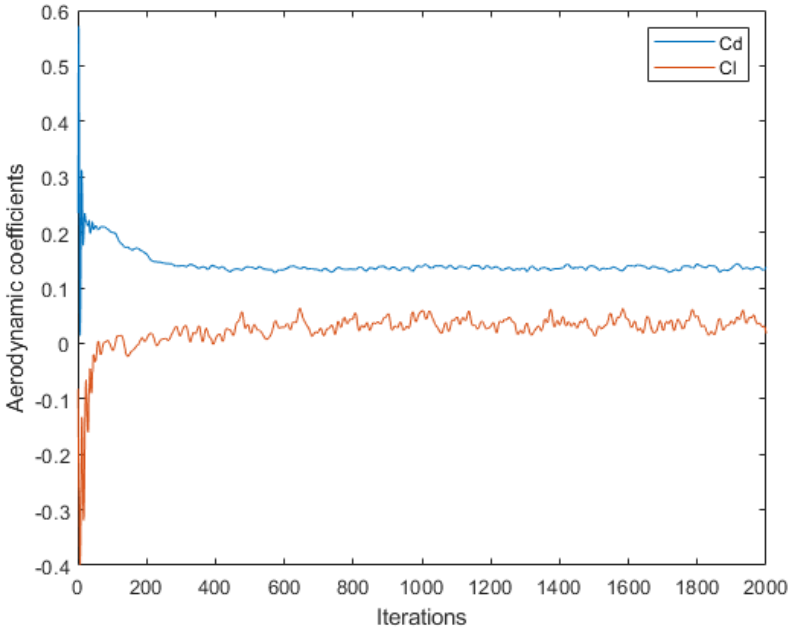

FIGURE 6.10: Aerodynamic coefficients from DrivAer VG type 2 configuration

With this second plot (see figure 6.10), it occurs the same as in the convergence graph, where no major differences in the variables' behaviour take place compared to the standard configuration (see figure 6.2). In both figures, some initial iterations are needed to get towards the mean value. In addition, observe how in the VG configuration, a small oscillation remains until the end of the plot regarding the lift coefficient. Meanwhile, in figure 6.2, this oscillations get slightly smoother towards the end. Finishing with the comparison, in figure 6.10 there is a difference of 0.1 regarding the C_l starting value. This fact occurs due to the algorithm's iterative solving, and does not affect the outcome.

Aerodynamic coefficients	VG type 2	Standard	Difference (%)
C_d	0.263	0.2606	0.921
C_l	0.0611	0.0788	22.462

TABLE 6.2: Aerodynamic coefficients comparison between VG type 2 and standard configurations

The values obtained from figure 6.10 are presented in table 6.2. From these values, several comments can be made. First of all, the Drag coefficient has increased in its third decimal (+0.003). This increase growth is minuscule if compared to the amount of new surface added by the installation of the VG. On the other hand, it is appreciated that C_l decreases its value by 22%. It was the behaviour desired, because the lift coefficient represents the upwards force of the car. A diminution means that downforce has been generated, being the resultant coefficient lower. Therefore, it can be stated that it is a positive tradeoff, from the aerodynamic point of view, the installation of a VG.

Now, where this lift and drag are generated is the following question. From a deductive perspective, the extra downforce should be appearing at the trunk/rear of the car, after the VG's location. In the same manner, the drag should materialize at the frontal surface of the VG, where it meets the airflow coming from the roof.

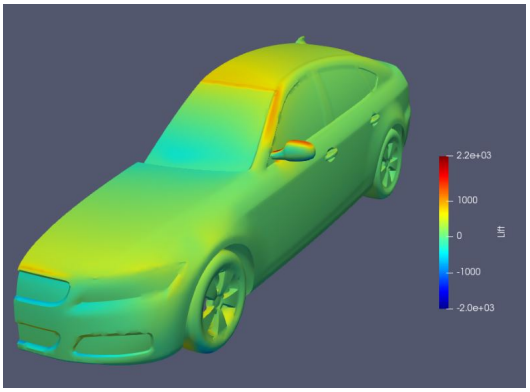

FIGURE 6.11: Lift generated over the DrivAer VG type 2 configuration surface, isometric view

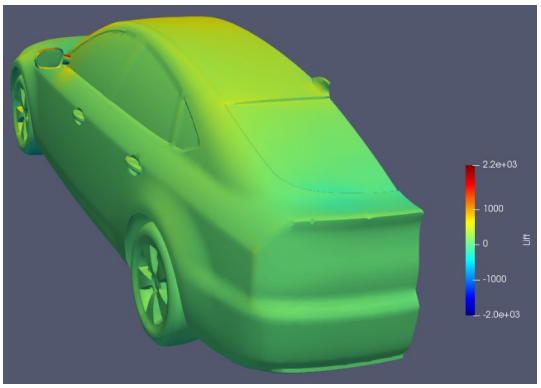

FIGURE 6.12: Lift generated over the DrivAer VG type 2 configuration surface, isometric rear view

As concerns to the lift, both figures 6.11 and 6.12 show a pretty similar configuration compared to the standard one. Downforce is generated on the same spots: frontal bumper, windshield and trunk. However, it can be appreciated that 6.12

has a wider light blueish area over the trunk/rear area, and that is the extra downforce generated by the VG.

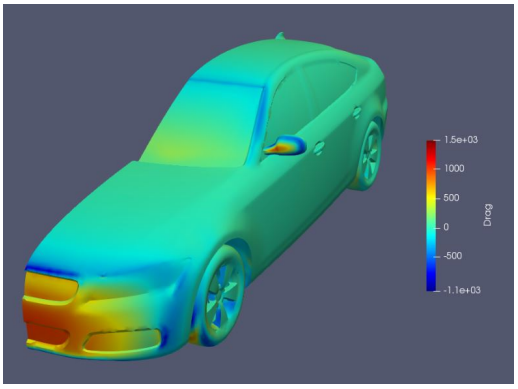

FIGURE 6.13: Drag generated over the DrivAer VG type 2 configuration surface, isometric view

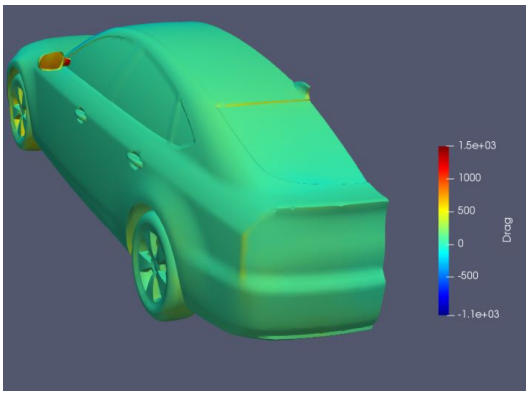

FIGURE 6.14: Drag generated over the DrivAer VG type 2 configuration surface, isometric rear view

From table 6.2 it could be expected that an increase of 0.003 regarding the drag coefficient is almost unnoticeable, and that is the case for figures 6.13 and 6.14. Despite that, it was not silly to think that the vortex generator frontal area could suffer a drag penalization, while the figures do not show that conduct. Two reasons are behind that fact: firstly, the drag increase is not large enough, which has already been mentioned. Secondly, and an important aspect later discussed at Chapter 7, the fastback configuration. If a frontal view was taken of the model, it could be appreciated that the VG does not emerge, meaning that the roof curvature covers it. Then, the airflow received by the aerodynamic element is not coming from free stream, it is already conditioned by the front surface of the car, mitigating the VG effect (including the drag generated by its own geometry).

As from the previous images the aerodynamic changes can barely be seen (only in figure 6.11 a wider downforce area is observed), the pressure coefficient distribution has been plotted over the car's length, just as with the standard configuration. For a better understanding, figure 6.15 is presented:

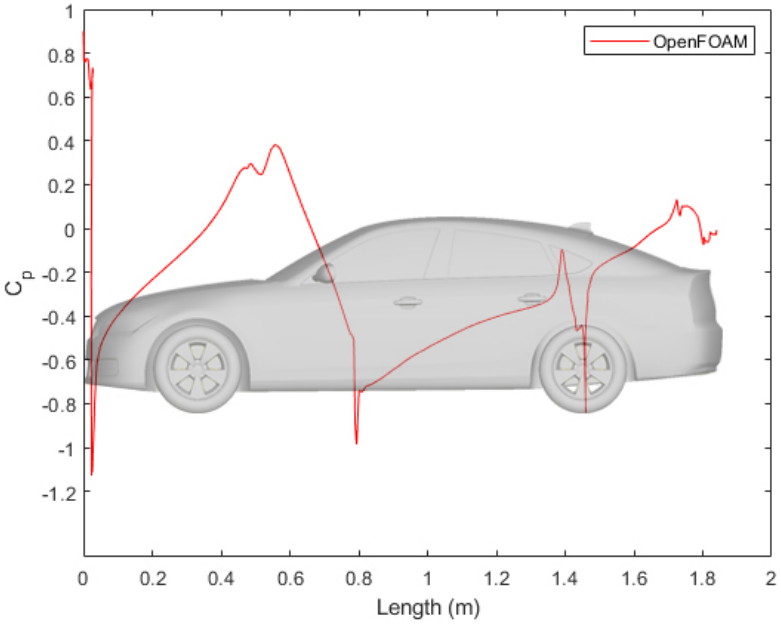

FIGURE 6.15: Pressure coefficient distribution over DrivAer VG type 2 configuration symmetry plane

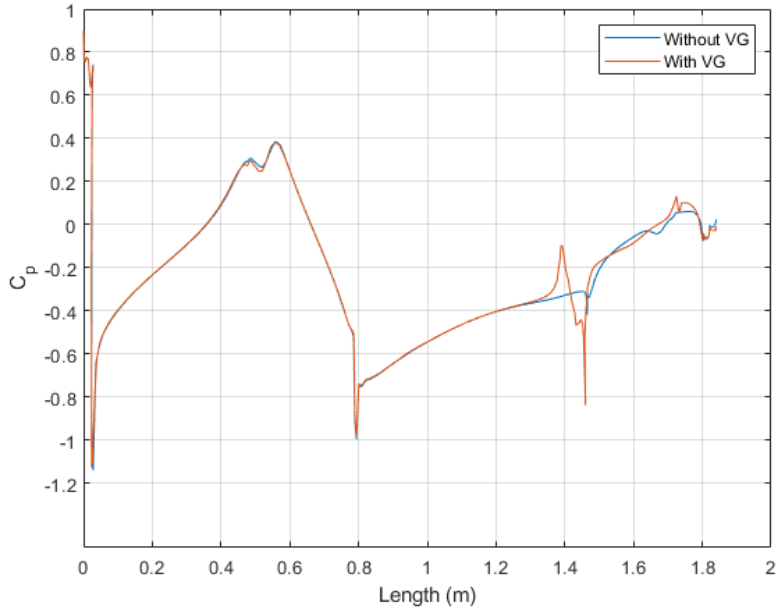

FIGURE 6.16: Pressure coefficient distribution comparison: DrivAer VG type 2 vs standard configuration

Moreover, figure 6.16 compares the results obtained for each configuration. Both

functions act the same way until VG is reached, approximately at 1.3 meters. There, when the airflow approaches the aerodynamic component, the flow's pressure grows suddenly, reaching a peak at 1.4 meters. Once the flow starts going over the VG's geometry, it begins to accelerate, which is translated directly in a pressure loss, arriving to a suction minimum. When the flow surpasses the totality of the VG' surface, a sudden expansion occurs, which is represented in that step formed just after the suction's minimum. It is important to highlight how the C_p's behaviour afterwards is much smoother and less oscillating than the standard configuration. Finally, the conduct of both functions is similar, having a last drop in pressure due to the surface shape change (from concave to convex) and both finally reaching the ambient pressure.

6.2.3 Thickness comparison: type 1 vs type 2

Along all this explanation, only the DrivAer VG type 2 configuration has been presented. The reason behind it is that this second design presents a better aerodynamic performance than the first one. Hence, the differences obtained with the installation of the VG are more pronounced and easier to appreciate. However, to get to that conclusion, both configurations were simulated. In this subsection, a brief explanation is performed to back up those affirmations, providing some data.

Regarding the values obtained for both coefficients, table 6.3 collects the data obtained from both simulations:

Aerodynamic coefficients	**VG type 1**	**VG type 2**	**Difference (%)**
C_d	0.275	0.263	4.36
C_l	0.0738	0.0611	17.208

TABLE 6.3: Aerodynamic coefficients comparison between VG type 1 and VG type 2 configurations

The results from this table show a parameter that is key in order to obtain the best aerodynamic performance, and that is thickness. In section 3.2 is explained that type 2 is achieved by reducing the fin's thickness by 1 cm each side. This variable is related to the frontal area the VG has. Therefore, less thickness implies less area, and results from table 6.3 demonstrate that less area translates to a better

aerodynamic performance. More precisely, notice how both coefficients improve notably by reducing the aerodynamic resistance and by generating downforce (drag and lift reduction respectively).

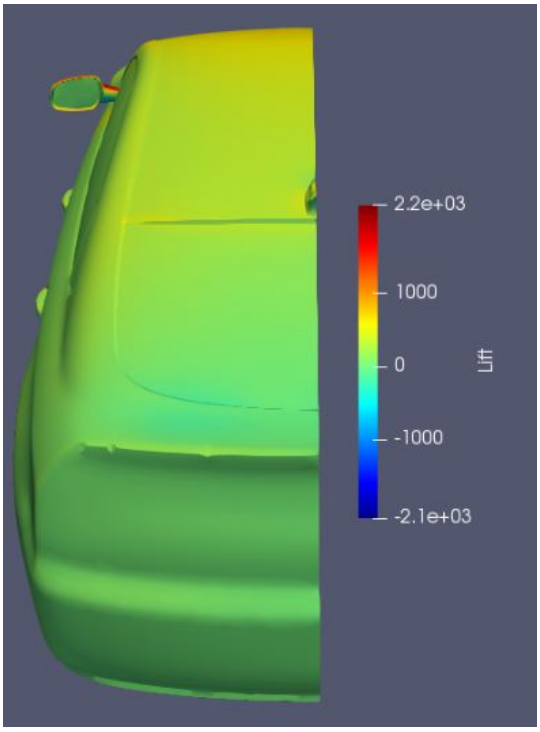

FIGURE 6.17: Lift generated over the DrivAer VG type 1 configuration, rear view

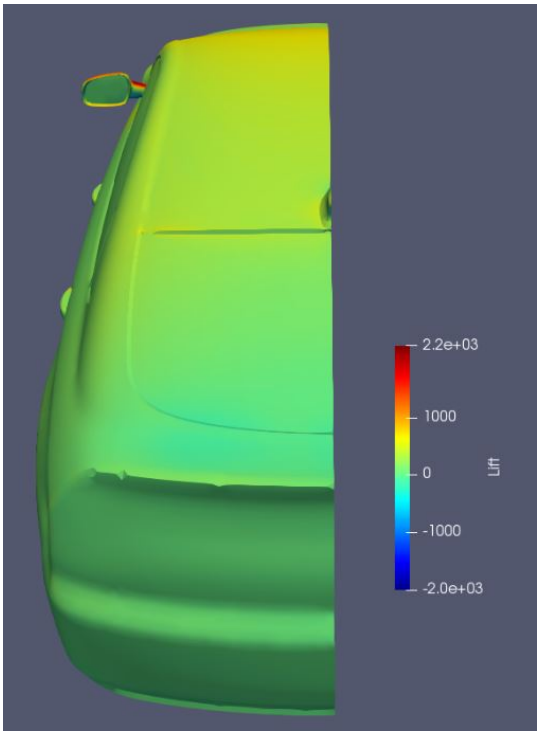

FIGURE 6.18: Lift generated over the DrivAer VG type 2 configuration, rear view

This downwards force increase can be seen perfectly in figures 6.17 and 6.18. Notice how in the figure of the right, the one representing the thinner VG, a wider blueish area is found, meaning that more negative lift (i.e. downforce) is generated. As for the drag is concerned, even though the vehicle has a slightly lighter color in figure 6.19 than in figure 6.20 (probably due to post-processing software parameters), the only remarkable difference is the back area of the VG, where the thicker configuration sees a higher drag because of its larger surface.

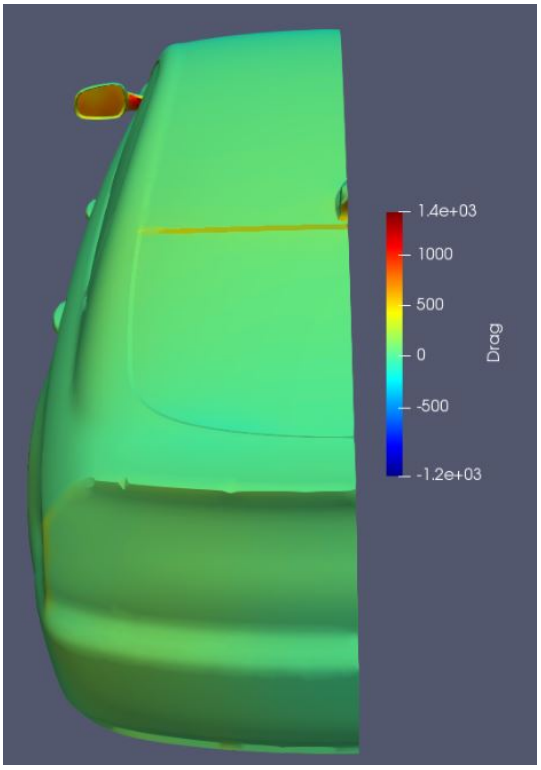

FIGURE 6.19: Drag generated over the DrivAer VG type 1 configuration, rear view

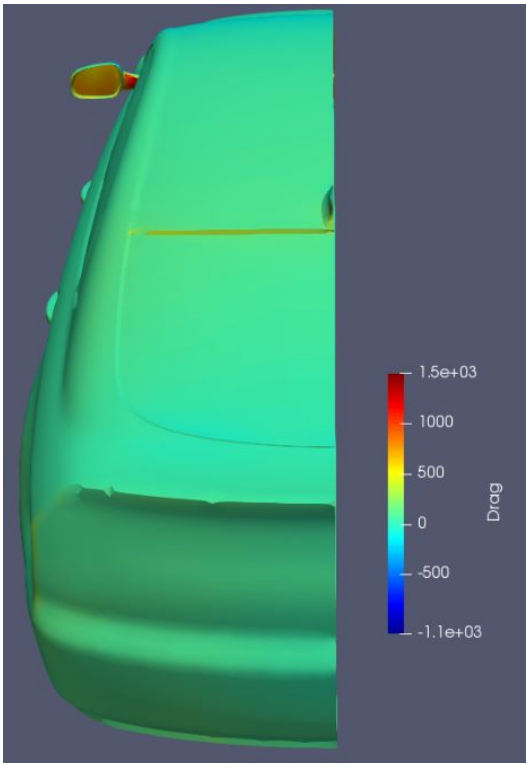

FIGURE 6.20: Drag generated over the DrivAer VG type 2 configuration, rear view

Chapter 7

Conclusions

This study can be splitted in two major parts. The first one concerns to the simulation of the DrivAer standard configuration, from which setup and turbulence model are chosen, through the simulation itself and right up to the comparison between experimental and numerical results. On the other hand, the second part has been the addition of a VG to the DrivAer configuration, and how it affects to its aerodynamic performance. In addition, two types of VG were designed, and a brief study of their effects depending on their thickness has been developed.

To sum up with the DrivAer standard configuration, it can be stated that the simulation captures the behaviour of the airflow fairly well. However, several comments are given regarding the pressure coefficient distribution in figure 6.8. As [14] establishes, the k-ω SST model under-predicts the pressure coefficient. In addition, it predicts too strong suction, but that deviation is not enough to explain the one obtained in those peaks. The author indicates that the best solution would be a better surface mesh refinement. Then, it is pointed out that the gap starting at 0.8 meters is due to the strut-based configuration used in the wind tunnel to hold the DrivAer's body. Therefore, the simulation, adding the modeling of the wind tunnel, would capture perfectly that area, having only the problematic of the suction peaks left. Hence, using the same initial conditions and turbulence model, only the surface mesh could be improved. Although those suction peaks are present, they can be disparaged, as they do not induce to an unrealistic behaviour of the airflow's totality. Proof of that are figures 6.3 and 6.4, where downforce is generated in areas such as the frontal bumper, the windshield and the trunk of

the vehicle, just where it is supposed to be. With all of this said, the author of this study believes that the outcome of the simulation is valid, being under a 5% error requirement.

Regarding the second part of this work, the effects of the VG installed over the car's roof have been successfully proven, understanding its function in car aerodynamics. As for the type 2 configuration (the thinner one), the C_d almost remained with the same value, while C_l was reduced up to 22%. Moreover, downforce was generated at the rear of the car, just after the VG's location, where it is supposed to appear (see figures 6.11 and 6.12). In figure 6.8, it can be appreciated how the airflow accelerates over the VG surface, decreasing the pressure coefficient in that area. Finally, a suction peak is found right at its end, followed by an expansion of the airflow as there is no more surface to stick to.

Aerodynamic coefficients	**Standard**	**VG type 1**	**VG type 2**
C_d	0.2606	0.275	0.263
C_l	0.0788	0.0738	0.0611

TABLE 7.1: Aerodynamic coefficients of each configuration

As for the type 1 configuration, table 7.1 shows how its installation increases the drag coefficient, meeting one of the main problems of the VG' setups: the drag produced by the component itself. Even though the C_l is reduced, it does not compensate this remarkable increment in aerodynamic resistance. Besides the tendency of reducing/increasing those coefficients, its is important to mention that the increments obtained match the reality, as [7] shows that the order of magnitude of those increases/decreases can go from 0.001 up to 0.01 (which meets the results of this study).

To conclude, it can be observed in table 7.1 that the addition of a VG can improve the aerodynamics of a car. Therefore, designers do not use them only as an aesthetic cover of the car's antenna, but for a better performance in general. However, it has been presented that this is not always the case. Its potential is affected by its thickness (frontal area in general): the thinner the VG is, the better for the vehicle's aerodynamic behaviour.

7.1 Future work

Once the vortex generators have proven its aerodynamic effects, multiple studies can be derived. For instance, knowing that the VG's design affects so much in its performance, the next logical step would be the design of a VG that maximizes the aerodynamics of a car. However, it is not as simple as it looks, because two major problem arise. One of them is the mechanical part, mainly because it has to withstand the loads from both aerodynamics and the ones produced by the dynamics of the car. Secondly, remember that the main reason of the VG's usage nowadays is to cover the car's antenna. Hence, a space limitation in its interior appears due to the space required by the electronic components.

Other possible studies could be to optimize the VG initial conditions. By that, the author refers to change certain variables such as velocity or the number of elements installed. Keep in mind that the current study has only taken into account one VG's behaviour for an airflow coming at 40 m/s, a relatively high speed that can only be achieved in motorways (depending on the regulations of each country). Then, it could be interesting how this aerodynamic component performs at lower speeds. Or, for example, what happens if the number of VGs is increased, installing a row of them instead of one (setup that is found in some planes).

Finally, the most complex work would be the study of the VG's positioning, and how it affects to the vehicle's performance. The difficulty here resides in all the possibilities existing, as not every VG is located on the roof, some of them are positioned in the rear lamps or next to the driver's window. In addition, this topic is related directly to the car's geometry. For instance, in this study, the DrivAer's fastback configuration has been chosen, and the VG has been located in the area where the surface curvature is higher. However, there are the estateback and the notchback configurations left, with more pronounced surfaces. Thus, a different study has to be done each time when a new vehicle s geometry is designed.

Chapter 8

Environmental impact

In this chapter, a study of the environmental impact generated throughout this work is presented. Due to COVID-19 exceptional circumstances, no displacements were made, being the electricity production the totality of the environmental impact. As in every other CFD-based study, the main power consumption comes from the computer used for the simulations. In this case, the computer's power supply has a power of 750W. In addition, as this work has been developed from September to January, workspace lighting was needed most of the time. Then, an estimation has been made, which is that 75% of the time the lights were on. With all of this information, and with the data provided by Endesa [39] (the largest electric utility company in Spain) of 2019, as the 2020 is not available yet, the environmental impact of this study is found in table 8.1:

Source	Time (h)	kW	kWh	Impact factor (kg CO2/kWh)	kg CO2
Computer's power supply	600	0.75	450	0.20	90
Workspace lighting	450	0.024	10.8	0.20	2.16
TOTAL					**92.16**

TABLE 8.1: Environmental impact originated throughout the study

Chapter 9

Budget

In this following chapter, an overview of the budget needed for the realization of this study is performed. The total costs can be broken down in two different areas: human resources and software required.

Regarding to the human resources, the cost of an engineer's hour varies drastically depending on each country. However, as this study has been developed in Spain, the Spanish mean cost of an engineer's hour will be the one chosen. Then, for this work specifically, the engineering work costs around 35 € per hour.

Now, moving to license's theme, most of the technical software used by engineers needs to be paid. During this study particularly, three licenses were needed:

- Microsoft Office 365: essential for using programs such as Microsoft Excel, there are several subscription options. For a 1 year student' subscription, the service costs 69 €. As the service has only been used for 5 months, the final cost is 28.75 € tax not included.
- Solidworks: software used for CAD design. As happened with Microsoft, Dassault Systems offer several Solidworks editions. In this case, the student version costs approximately 150 € [40] and works for one year. Therefore, using it only for 5 months, its cost reduces to 62.5 € tax not included.
- Matlab: required for post-processing and plotting. The student suite license costs 69 € per year. Then, the final cost is 28.75 € tax not included for a 5 months usage.

Once each expense has been detailed, table 9.1 presents the total budget needed for this work, adding 21% from VAT:

Source	**Time (h)**	**Hourly rate (€/h)**	**Power (kWh)**	**Electricity fee (€/kWh)**	**Cost (€)**
Electrical supply	600	-	460.8	0.1199	55.25 €
Human resources	600	35	-	-	21,000.00 €
Software					
Office 365	-	-	-	-	28.75 €
Solidworks	-	-	-	-	62.50 €
Matlab	-	-	-	-	28.75 €
Subtotal (VAT not included)					21,175.25 €
VAT (+21%)					4,446.81 €
TOTAL					**25,622.06 €**

TABLE 9.1: Total budget of the study

Chapter 10

Planning

One of the crucial aspects of any study is its planning. The purpose of a planning study is to accomplish the project objectives within the deadlines specified in the most efficient way. In order to do so, all the tasks that will be carried out have to be detailed before starting. For a better understanding, table 10.1 is presented:

Task	**Description**
1	**Project management**
1.1	Project charter
1.2	Memory writing
1.3	Project review
2	**Research and development**
2.1	Papers research
2.2	DrivAer: geometry assembly
2.3	ANSA: geometry preparation
2.4	Mesh generation
2.5	Simulation
2.6	Vortex generator design
2.7	Mesh optimization
2.8	Post-processing
3	**Know how**
3.1	ANSA: formation

TABLE 10.1: Task list

The following move is to sort them in such a manner that the shortest way possible of execute them all is obtained. For this reason, table 10.2 is presented, where for each task its precedent is detailed. With this method, the crucial steps (i.e. tasks which many others depend on) are now visible, and the optimal path is revealed:

Task	**Description**	**Precedent**
1	**Project management**	
1.1	Project charter	2.1
1.2	Memory writing	2.6
1.3	Project review	1.2
2	**Research and development**	
2.1	Papers research	-
2.2	DrivAer: geometry assembly	1.1
2.3	ANSA geometry preparation	2.2, 3.1, 2.6
2.4	Mesh generation	2.3
2.5	Simulation	2.4
2.6	Vortex generator design	1.1
2.7	Mesh optimization	2.5
2.8	Post-processing	2.6
3	**Know how**	
3.1	ANSA formation	-

TABLE 10.2: Task list organization

Moreover, a Gantt chart can be found in figure 10.1 for a better visualization of each task timeline:

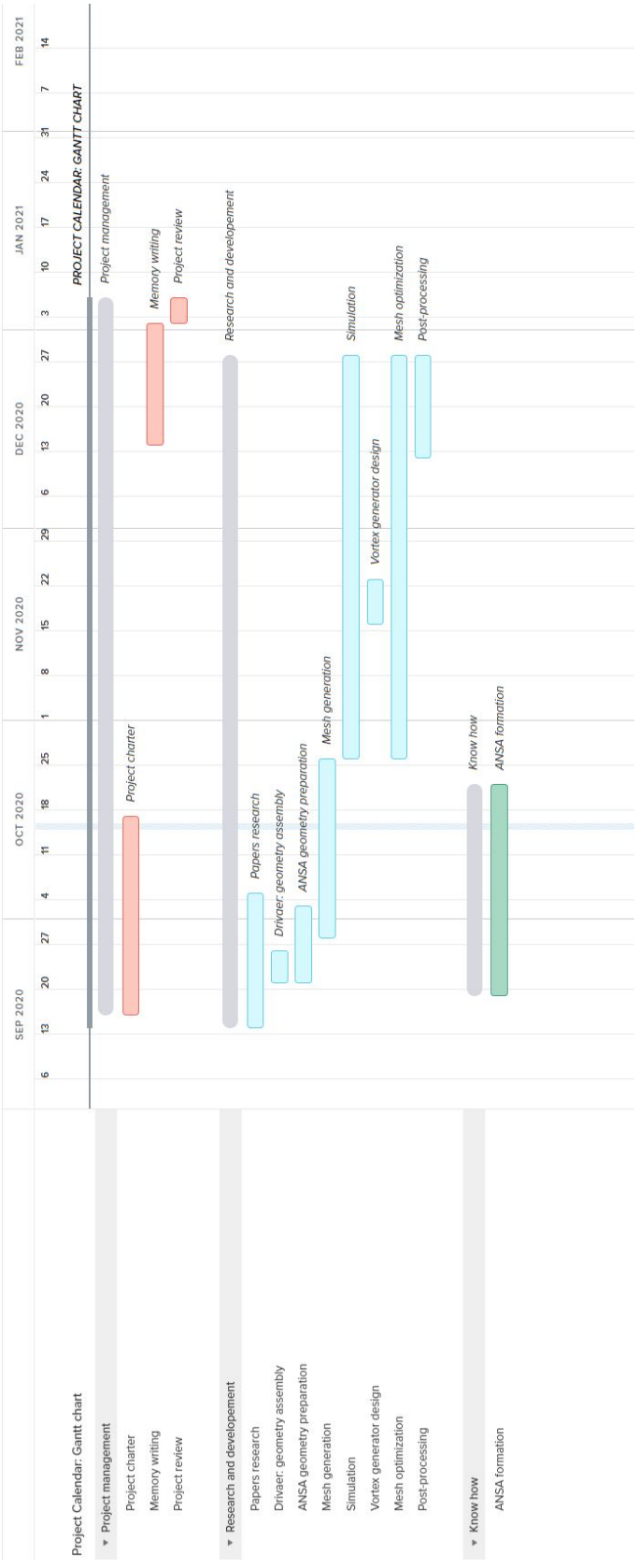

FIGURE 10.1: Gantt chart

To sum up with this chapter, figure 10.2 shows the hours destined for this project per week. Then, the totality of hours worked in this study is around 600 hours.

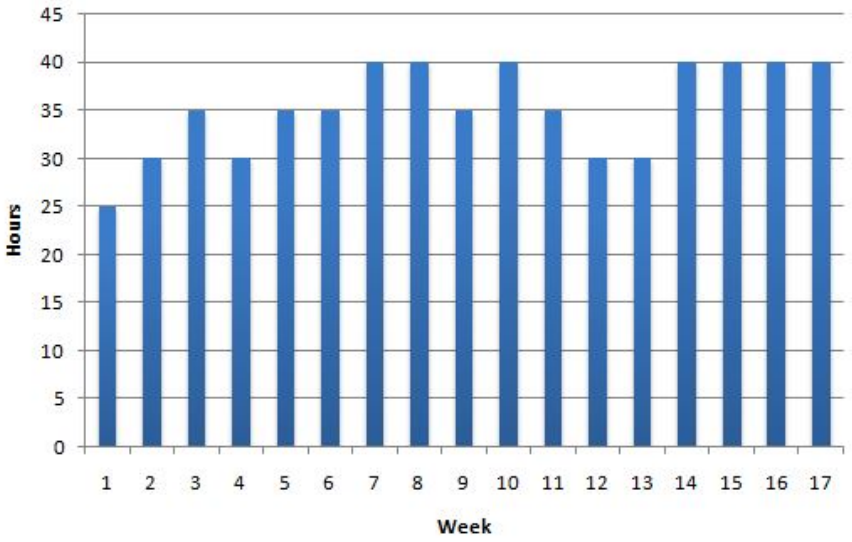

FIGURE 10.2: Hours worked per week estimation

Bibliography

[1] Mercedes-Benz, "Mercedes-benz public archive." "https://mercedes-benz-publicarchive.com/marsClassic". [Retrieved on 14-11-2020].

[2] SimScale, "What is aerodynamics?." "https://www.simscale.com/docs/simwiki/cfd-computational-fluid-dynamics/what-is-aerodynamics/". [Retrieved on 21-11-2020].

[3] Maxton Design, "Front splitter audi s1 8x." "https://maxtondesign.com/product-eng-8416-Front-Splitter-Audi-S1-8X.html". [Retrieved on 25-11-2020].

[4] Verus Engineering, "Dive planes and canards." "https://www.verus-engineering.com/blog/new-product-11/post/dive-planes-and-canards-38". [Retrieved on 25-11-2020].

[5] SSDD Motorsport, "Bmw carbon side skirt." "https://www.ssdd-motorsport.com/f80-m3-f82-m4-performance-look-carbon-side-skirt-extensions/". [Retrieved on 26-11-2020].

[6] Grassroots Motorsports, "Downforce sorcery: Diffusers explained." "https://grassrootsmotorsports.com/articles/downforce-sorcery-diffusers-explained/". [Retrieved on 19-12-2020].

[7] Koike, M., "Research on Aerodynamic Drag Reduction by Vortex Generators," 2004. [Retrieved on 19-12-2020].

[8] Jpcarbon, "Carbon Fiber Roof Spoiler Vortex Generator for 2008-2010 Mitsubishi EVO." "http://jpcarbon.com/Carbon-Fiber-Roof-Spoiler-Vortex-Generator-for-2008-2010-Mitsubishi-EVO-10-EVO-X-P2097219.aspx/". [Retrieved on 19-12-2020].

[9] Heft, Angelina I. and Indinger, Thomas and Adams, Nikolaus A., "Introduction of a New Realistic Generic Car Model for Aerodynamic Investigations," 2012. [Retrieved on 26-12-2020].

[10] SimScale team, "What is y+(yplus)?." "https://www.simscale.com/forum/t/what-is-y-yplus/82394". [Retrieved on 28-12-2020].

[11] BETA CAE Systems, "External Aerodynamics: hybrid volume mesh." "http://dma.ing.uniroma1.it/users/paciorri/external_aero.pdf". [Retrieved on 27-12-2020].

[12] BETA CAE Systems, "ANSA for CFD Quick Start Guide." "http://oss.jishulink.com/caenet/forums/upload/2013/04/18/380/141830597704821.pdf". [Retrieved on 28-12-2020].

[13] Gorde, A., "Conjugate Heat Transfer for Electronic Cooling using OpenFoam," 2015. [Retrieved on 30-12-2020].

[14] Ashton et al., "Assessment of RANS and DES methods for realistic automotive models," 2016. [Retrieved on 21-12-2020].

[15] Wikipedia, "Automotive aerodynamics." "https://en.wikipedia.org/wiki/Automotive_aerodynamics". [Retrieved on 14-11-2020].

[16] Ortega, E., "Aerodynamic forces, aerodynamics lecture notes."

[17] Formula 1 Dictionary, "Splitters and air dam." "http://www.formula1-dictionary.net/splitter.html#:~:text=Front%20splitters%20are%20essential%20aerodynamic,bottom%20of%20the%20front%20bumper.". [Retrieved on 24-11-2020].

[18] WRC Wings, "Underbody aerodynamics of the 2017 wrc cars." "https://www.wrcwings.tech/2017/10/20/underbody-aerodynamics-of-the-2017-wrc-cars/". [Retrieved on 26-11-2020].

[19] Stojanović, N., "Effect of Rear Spoiler Shape on Car Aerodynamics and Stability," 2020. [Retrieved on 21-12-2020].

[20] Hesselgreaves, J., "Compact Heat Exchangers (Second Edition)," 2017. [Retrieved on 19-12-2020].

[21] Wikipedia, “Navier-Stokes equations.” "https://en.wikipedia.org/wiki/Navier%E2%80%93Stokes_equations". [Retrieved on 21-12-2020].

[22] Gámez, P. J., “Ec. Navier Stokes, Fluid Mechanics Class Notes,” 2018. [Retrieved on 21-12-2020].

[23] NASA, “Navier-Stokes equations.” "https://www.grc.nasa.gov/www/k-12/airplane/nseqs.html". [Retrieved on 21-12-2020].

[24] Turbulence and Aerodynamics Research Group (TUAREG), “RANS modelling, Advanced Aerodynamics Class Notes,” 2020. [Retrieved on 28-12-2020].

[25] Castilla, R., “Turbulence modeling in OpenFOAM, CFD Class Notes,” 2020. [Retrieved on 21-12-2020].

[26] Wasserman, S., “Choosing the right turbulence model for your CFD simulation.”.” "https://www.engineering.com/DesignSoftware/DesignSoftwareArticles/ArticleID/13743/Choosing-the-Right-Turbulence-Model-for-Your-CFD-Simulation.aspx". [Retrieved on 21-12-2020].

[27] Wikipedia, “Menter’s Shear Stress Transport (SST).” "https://en.wikipedia.org/wiki/Menter%27s_Shear_Stress_Transport". [Retrieved on 21-12-2020].

[28] NASA, “Turbulence Modeling Resource.” "https://turbmodels.larc.nasa.gov/". [Retrieved on 21-12-2020].

[29] Technische Universität München, “DrivAer Model.” "https://www.mw.tum.de/en/aer/research-groups/automotive/drivaer/". [Retrieved on 26-12-2020].

[30] Fernie, Mike, “How is a car’s drag coefficient calculated?.” "https://drivetribe.com/p/how-is-a-cars-drag-coefficient-RUb1vQtoTlyeBW9yR7fmRw?iid=fXrmZc7lTf-URhgyz3iE7w". [Retrieved on 26-12-2020].

[31] BETA CAE Systems, “ANSA pre processor.” "https://www.beta-cae.com/ansa.htm". [Retrieved on 27-12-2020].

[32] Shinde, G., “Numerical Investigations of the DrivAer Car Model using Open-source CFD Solver OpenFOAM,” 2013. [Retrieved on 27-12-2020].

[33] LearnCAx, “Basics of Y Plus, Boundary Layer and Wall Function in Turbulent Flows.” "https://www.learncax.com/knowledge-base/blog/by-category/cfd/basics-of-y-plus-boundary-layer-and-wall-function-in-turbulent-flows". [Retrieved on 27-12-2020].

[34] Turbulence and Aerodynamics Research Group (TUAREG), “Near wall refinement, Mesh considerations Class Notes,” 2020. [Retrieved on 28-12-2020].

[35] Wikipedia, “OpenFOAM.” "https://en.wikipedia.org/wiki/OpenFOAM". [Retrieved on 30-12-2020].

[36] OpenFOAM team, “The open source CFD toolbox.” "https://www.openfoam.com/". [Retrieved on 30-12-2020].

[37] CFD online team, “Turbulence length scale.” "https://www.cfd-online.com/Wiki/Turbulent_length_scale". [Retrieved on 30-12-2020].

[38] CFD online team, “Turbulence free-stream boundary conditions.” "https://www.cfd-online.com/Wiki/Turbulence_free-stream_boundary_conditions". [Retrieved on 30-12-2020].

[39] Comision Nacional de los Mercados y la Competencia, “Información sobre su electricidad.” "https://gdo.cnmc.es/CNE/resumenGdo.do?anio=2019". [Retrieved on 31-12-2020].

[40] EngineeringClicks team, “SolidWorks Price Guide: How much does it cost to buy SolidWorks.” "https://www.engineeringclicks.com/solidworks-price-guide/#:~:text=SolidWorks%20Student%20price&text=For%20students%2C%20they%20offer%20a,purchased%20directly%20through%20the%20website.". [Retrieved on 31-12-2020].

Declaration on honour

I declare that,

- The work in this Degree Thesis is completely my own work.
- No part of this Degree Thesis is taken from other people's work without giving them credit.
- All references have been clearly cited.

I understand that an infringement of this declaration leaves me subject to the foreseen disciplinary actions by *The Universitat Politècnica de Catalunya - BarcelonaTECH.*

Title of the thesis: Study of the passive flow control mechanism applied to a generic (DrivAer) car.